https://doi.org/10.5194/egusphere-2026-3790
Preprint. Discussion started: 6 August 2026

The Ground-based Fog and Aerosol Spectrometer - Technical description and first applications

Lea Haberstock[1,2], Darrel Baumgardner[3], Dagen D. Hughes[3], Julie Legrand[1,4], Almuth Neuberger[1,2], Cuiqi Zhang[5], Zamin A. Kanji[5], Christian Maier[6], Ilona Riipinen[1,2], Radovan Krejci[1,2], and Paul Zieger[1,2]

[1]Department of Environmental Science, Stockholm University, Stockholm, Sweden
[2]Bolin Centre for Climate Research, Stockholm University, Stockholm, Sweden
[3]Droplet Envea Group, Longmont, CO, USA
[4]ESPCI Paris-PSL, Paris, France
[5]Institute of Atmosphere and Climate Science, D-USYS, ETH Zürich, Zürich, Switzerland
[6]GeoSphere Austria, Vienna, Austria

Correspondence: Paul Zieger (paul.zieger@aces.su.se)

Abstract. High-precision measurements of cloud microphysical properties, such as particle size and phase, remain challenging. The most common method for in-situ single-particle measurements is via light scattering, where size is inferred from the scattered-light intensity using Mie-Lorenz theory. Here, we present the newly developed instrument, the Ground-based Fog and Aerosol Spectrometer (GFAS). Besides particle size and number concentration obtained from forward-scattering measurements, the GFAS also measures the change in polarization of backward scattered light, which allows for investigating particle morphology and composition. Within this work, we present a new methodology to calibrate detectors of light scattering spectrometers using a poly-disperse spray of pure water coupled with theoretical Mie-Lorenz modeling. Furthermore, we show the importance of proper calibration procedures to derive reasonable and interpretable data with respect to particle size and degree of linear polarization. In particular, we show that the new autocalibration method that uses a spray of pure water droplets leads to lower uncertainties compared to the standard glass bead calibration and is also usable for the polarized backward scattering detectors. Finally, we evaluate the GFAS using laboratory and field measurements. Under laboratory conditions, polarization measurements distinguish water droplets from nonspherical dust. Under ambient conditions, however, this distinction becomes considerably more challenging. For the in-situ observations, we find that cloud particle optical properties are distinctly different compared to those of pure water measured under laboratory conditions, indicating a potentially elevated refractive index in cloud droplets compared to pure water.

https://doi.org/10.5194/egusphere-2026-3790
Preprint. Discussion started: 6 August 2026

1 Introduction

Cloud properties like hydrometeor size, composition, and shape are difficult to measure with high accuracy, and results differ strongly depending on the measurement principle (Baumgardner, 1983; Burnet and Brenguier, 1999; Spiegel et al., 2012). In particular, mixed-phase clouds often lack representativeness in studies, although the differentiation between liquid and ice is critical for determining their optical properties and the evolution of precipitation (Korolev et al., 2017).

Optical measurement techniques are among the primary methodologies used to measure properties of clouds. Since the late 1970's, a range of different instruments has been developed for the in-situ measurements of cloud hydrometeors (Knollenberg, 1976; Baumgardner et al., 2011). Cloud measurements are primarily performed via two in-situ strategies: sensors on airborne platforms (e.g., aircrafts, balloons, drones), providing vertical and horizontal profiling; and ground-based instruments (Gultepe et al., 2014; Shupe et al., 2008; Doulgeris et al., 2020), enabling continuous sampling on longer temporal scales (Gayet et al., 1996; Baumgardner et al., 2011). Larger particles like cloud drops, drizzle or snowflakes (diameter 10^1-10^3 µm) can be analyzed through imaging (Baumgardner et al., 2011) and holographic methods (Fugal et al., 2004), while smaller particles (coarse aerosols and cloud droplets; 100's nm to 100's μm) are usually measured via single-particle light scattering (e.g., Rosenberg et al., 2012; Tiitta et al., 2022; Um and McFarquhar, 2011). The principle of single-particle light scattering is based on Mie-Lorenz theory (Mie, 1908; Lorenz, 1890) in which a spherical particle, around the size of the wavelength of the incident light, scatters light according to the particle's size and refractive index ($m = n+ki$). By using a monochromatic light source, typically a laser, to illuminate particles and measuring the scattered light intensity with a detector, the size of a particle can be derived. The first commercially available single-particle light scattering spectrometer, the Axially Scattering Spectrometer Probe, was developed in the mid-1970s (ASSP; Pinnick and Auvermann, 1979). Since then, a range of other light scattering instruments has been developed that use similar techniques. While the Forward Scattering Spectrometer Probe (FSSP; Knollenberg, 1976; Miles et al., 2000), the Cloud Droplet Probe (CDP; e.g. McFarquhar et al., 2007) and the Fog Monitor (FM model 100 or 120; e.g. Spiegel et al., 2012) measure droplets only via forward scattering, there are also instruments that detect light scattered over more than one collection angle, e.g., the Small Ice Detectors (SID model 1 and 2; Cotton et al., 2010) and the Light Optical Aerosol Counter (LOAC; Renard et al., 2016) or by detecting polarized components of the scattered light, like the Cloud and Aerosol Spectrometer with Polarization (CASPOL; Glen and Brooks, 2013). Instruments with more than one collection angle can provide additional information about the scattering phase function of a particle, which allows the discrimination between spherical and nonspherical particles. The SID, for example, was designed to explicitly differentiate between ice crystals and droplets by measuring the phase function over several collection angles (Cotton et al., 2010), whereas the LOAC categorizes different types of aerosols by measuring in a forward and a sideward collection angle (Renard et al., 2016). Instruments measuring over the near forward and backward collection angles have been used to derive the refractive index of particles in the atmosphere by relating the ratio between the two scattering intensities to the refractive index (Baumgardner et al., 1996). Using a change in polarization of the backscattered light has been developed in the remote-sensing community to discriminate ice from liquid clouds by exploiting that nonspherical particles change the polarization angle of a linearly or circularly polarized laser more than spherical particles (e.g., Schotland et al., 1971; Korolev et al., 2017). A similar method has been developed for

https://doi.org/10.5194/egusphere-2026-3790
Preprint. Discussion started: 6 August 2026

in-situ measurements where the change in polarization is measured using two different detectors in the backward scattering, of which at least one has an optical mask in order to discriminate between the perpendicularly polarized and the parallel polarized light components with respect to the polarization of the laser (Baumgardner et al., 1996, 2011; Glen and Brooks, 2013, 2014).

The aim of this work is to present and characterize a new instrument development, the Ground-based Fog and Aerosol Spectrometer (GFAS, Envea, France). The GFAS follows the measurement principle of the FM, but it has two additional detectors in the near backward scattering region; one detector for the parallel polarized light component and one for the perpendicularly polarized light component with respect to the laser. With first laboratory and field measurements, we will show (1) how the GFAS performed during a field campaign at Sonnblick Observatory (SBO), Austria, focusing on its new feature, the polarized back-scatter measurements, and (2) how we can use these polarized back-scattering measurements to learn more about particle morphology and potentially the particle type. Additionally, a new method for auto-calibrating light scattering spectrometers is presented to avoid issues arising with glass bead calibrations. Furthermore, an algorithm correcting for particle sampling losses was developed specifically for the new GFAS.

2 Methodology

2.1 Technical description

The GFAS (Fig. 1) is a ground-based, single-particle light scattering spectrometer that derives particle size and approximates particle shape in the range of 0.95 - 50 μm (the lower size threshold might depend on the specific GFAS unit; for technical details, see Tab. 1). The air flow, temperature, and a set of diagnostic parameters are continuously monitored to assess the operational status of the instrument. Since sampling efficiency is highly dependent on the angle between wind direction and inlet orientation (Spiegel et al., 2012), the GFAS was designed to turn horizontally into the ambient wind by measuring the wind direction with an anemometer and adjusting its orientation.

Table 1. Technical specifications of the GFAS. For determination of particle coincidence probability, see Appendix C.

Laser wavelength λ	660 nm
Sampling frequency	Single-particle & 1 Hz output
Particle coincidence probability	$< 20\,\%$ for $N < 1000\,\mathrm{cm}^{-3}$
Inlet diameter	50.07 mm
Contraction part length	120.05 mm
Wind tunnel length until laser	143.54 mm
Wind tunnel diameter	25.04 mm
Sampling volume flow rate	around $5\,\mathrm{cm}^3\,\mathrm{s}^{-1}$
Light collection angles (forward, backward)	$3.8 - 20°$, $168 - 176.5°$
Laser cross section	$0.22\,\mathrm{mm}^2$

https://doi.org/10.5194/egusphere-2026-3790
Preprint. Discussion started: 6 August 2026

The optical components consist of a 660 nm diode laser that projects a collimated, focused light beam across the sampled airstream and lenses that collect some fraction of the forward and backward scattered light (see Fig. 1). When a particle crosses the laser beam, it scatters the incident light with an intensity depending on its size, shape, and refractive index, as well as the intensity and wavelength of the laser. The forward scattered light is collected over a solid angle of $3.8 - 20\,^{\circ}$ and is separated into two components with a beam splitter. One component is directed onto an Avalanche Photo Detector (APD) whose output signal is processed to derive a particle size. By assuming that the particle is spherical with a known refractive index, this scattering intensity can be converted into an equivalent optical diameter (d_{opt}) according to Mie-Lorenz theory (Mie, 1908; Lorenz, 1890). This detector is called the "sizer". The other component is projected onto a second APD through an optical mask, called the "qualifier", which restricts light from particles that pass through the beam outside of the Depth Of Field (DOF). The backscattered light, collected over a solid angle of $168 - 176.5\,^{\circ}$is also separated with a beam splitter into two components that are then directed onto APDs. Each APD has a linear polarizing filter, one oriented parallel to the incident laser light and the other oriented perpendicular to the incident laser light polarization (see Fig. 1).

2.2 Laboratory characterization

Measurements of water droplets and various solid, nonspherical particle samples were made in the laboratory to characterize the response of the GFAS scattering intensities I_{F}, $I_{\parallel}$, and $I_{\perp}$ of the corresponding detectors. Measurements of pure deionized water droplets and glass beads were also used to determine the scale factors c_i required to calibrate these detectors. The glass beads used were of sizes 2, 5, 8, 15, and 30 μm (Thermo Scientific, Duke Standards, borosilicate glass for 2-15 μm $n = 1.56$ and lime glass for 30 μm, $n = 1.51$ at 589 nm). All detector signals were calibrated using the theoretical σ calculated for the GFAS specific collection angles and wavelength (see Sect. 4.1).

Dust samples (volcanic dust extracted from the base of the Japanese Sakurajima volcano) were aerosolized with a self-made aerosol shaker and introduced into the GFAS inlet. To generate airborne cellulose fibers, tissue paper (paper hand towel roll, Katrin) was mechanically crumpled in close proximity to the sampling inlet. In addition, 15 μm glass beads (Thermo Scientific, Duke Standards, Borosilicate glass microspheres, $n = 1.56$ at 589 nm, mean diameter $14.6 \pm 2.3\,\mu$m) were dispersed into the instrument using the GFAS calibration kit (provided by the manufacturer). Water droplets were generated using deionized water and a commercially available medicare humidifier (Vicks, model WUL460E4, Switzerland).

2.3 Field deployment at Sonnblick Observatory, Austria

The Sonnblick Observatory (SBO) consists of two research sites: one is on the summit of Mt. Hoher Sonnblick (47.05° N, 12.96° E, 3106 m a.s.l.), Austria, and the other is at the mountain base. The station on the summit has two terraces situated on the northeastern edge of a steep escarpment descending into the valley below. In August 2024, the European Center for Cloud Ambient INTer-comparison (ECCINT), based at SBO, conducted an inter-comparison campaign focused on in-situ cloud measurements on the summit of Mt. Hoher Sonnblick. The instruments deployed included the GFAS, Fog Monitors (FM100, Droplet Measurement Technologies, USA), and Particulate Volume Monitor (PVM; Model PVM-100, Gerber Scientific Inc., USA), operated by various research groups. All instruments were located at the southeastern corner of the measurement terrace.

https://doi.org/10.5194/egusphere-2026-3790
Preprint. Discussion started: 6 August 2026

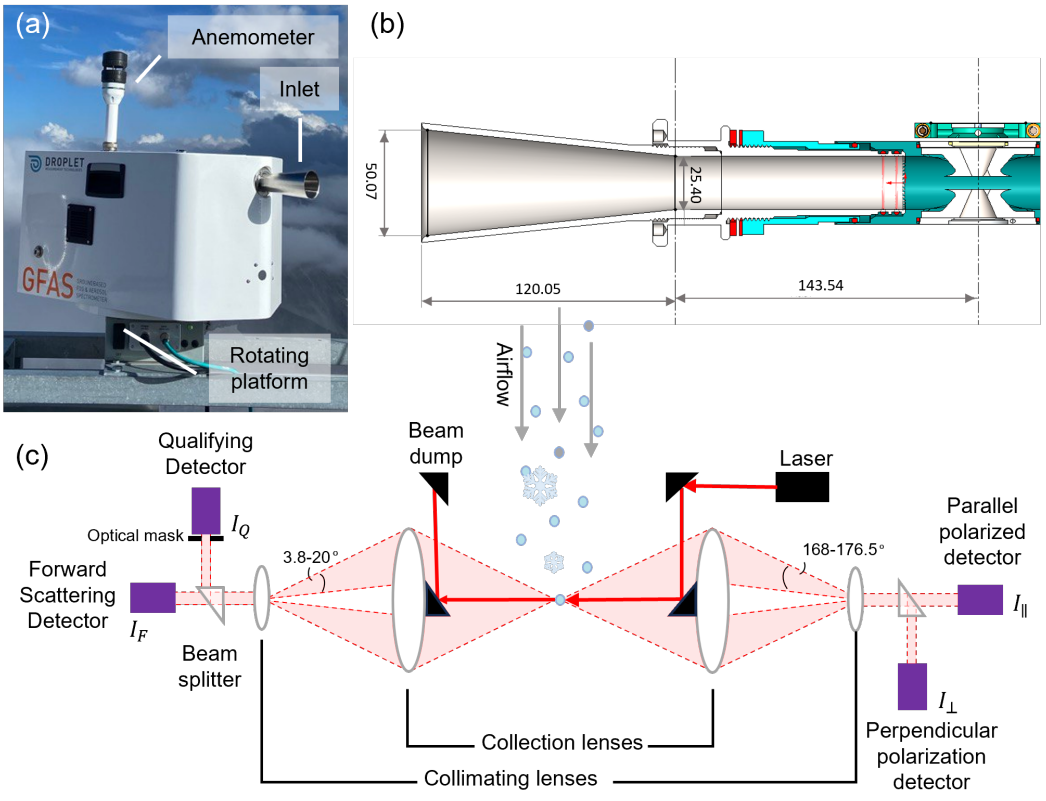

Figure 1. The ground-based fog and aerosol spectrometer (GFAS). (a) Photograph of GFAS at Mt. Sonnblick (Austria), (b) dimensions of instrument inlet (in mm), and (c) optical measurement principle. Cloud droplets, aerosols (blue and gray dots), and ice crystals are pulled through the wind tunnel, passing a laser beam. The scattered light (red) is directed via collection and collimating lenses towards the four detectors. I_i indicate the different signal intensities measured by the GFAS at each detector.

The PVM, which measures light forward scattered from ensembles of particles (Gerber, 1991), was mounted on the eastern side of the terrace, while the single-particle spectrometers (GFAS and FM) were mounted on the southern corner. While GFAS and PVM were approximately at the same height (1.5 m above the terrace ground), the FM was mounted in a more elevated position on a pole that could be manually turned into the main wind. GFAS and FM were approximately 1.7 m apart, while the PVM was approximately 2 m away from the GFAS. Aerosol optical properties were measured with a Polar Nephelometer Aurora 4000 (Schauer and Maier, 2020). The single scattering albedo (SSA) was calculated from the measured particle scattering and absorption coefficients (μ_{sp}, μ_{ap}, respectively). Its wavelength dependence was fitted with a power-law function to derive the SSA exponent (α_{SSA}). A change in the sign of α_{SSA} indicates an inversion of the Single Scattering Albedo (SSA) spectral dependence and is considered a marker of mineral dust influence (Collaud Coen et al., 2004).

https://doi.org/10.5194/egusphere-2026-3790
Preprint. Discussion started: 6 August 2026

2.4 Estimation of optical measurement uncertainties

The accuracy of the size and number concentration derived from single-particle light scattering optical spectrometers is impacted by uncertainties and limitations imposed primarily by two factors: 1) Uncertainty in the setup of the optical detection system and 2) natural variability in the cloud and aerosol optical properties (due to changes in refractive index and particle shape). An error estimate was performed using uncertainty propagation analysis through Monte Carlo simulations. We found that the error in sizing can be between 16-102 % for particles $\leq 12\,\mu$m and up to 18% for particles $>12\,\mu$m (for more details see Appendix C). The sensitivity in sizing is primarily introduced through the non-monotonic nature of Mie-Lorenz theory, which exhibits the strongest oscillations at sizes smaller than $12\,\mu$m.

3 Theoretical calculations

To assess the theoretical sensitivity of the GFAS to particle properties, the scattering cross sections of the forward scattered (σ_F), backward scattered parallel polarized ($\sigma_\parallel$), and backscattered perpendicular polarized ($\sigma_\perp$) components were modeled as a function of particle diameter for a range of different real ($n = 1.33 - 1.6$) and complex ($n = 1.33, k = 0 - 0.02$) refractive indices ($m = n + ki$) using Mie-Lorenz theory and the GFAS optical setup (see Fig. 2 and Fig. 3). The ranges of values were chosen based on those found in ambient aerosols (Zhao et al., 2020). These calculations were performed using the python package PyMieScatt (Sumlin et al., 2018) based on the algorithms of Bohren and Huffman (1998).

Although the scattering cross sections have a clear dependence on particle diameter, with an approximate power-law increase (see Figs. 2 and 3), there are distinct oscillations in the size-to-signal relationship, i.e., particles with different diameters can yield identical σ, introducing sizing uncertainties. An increase in the real part n of the refractive index significantly decreases the σ_F, particularly at larger diameters. This will lead to the under-sizing of particles with a higher refractive index than water. When changing the imaginary part of the simulated σ, signals for both forward and backward directions are dampened drastically, leading to potentially strong under-sizing with absorbing matter present (see Fig. 3).

The σ and its polarized components, $\sigma_\perp$ and $\sigma_\parallel$, are highly sensitive to the refractive index, size, and shape of the scattering particle. The degree of linear polarization r_{pol}, defined as

$$r_{\mathrm{pol}} = \frac{\sigma_\perp - \sigma_\parallel}{\sigma_\parallel + \sigma_\perp}, \tag{1}$$

can thus be used to infer information about the particle's morphology and composition (with the refractive index as an indicator for composition). For one, nonspherical particles change the polarization of a polarized laser more than a fully spherical particle (Korolev et al., 2017; Liou, 2002). Comparing therefore $\sigma_\perp$ to $\sigma_\parallel$ or the total backward scattering ($\sigma_B = \sigma_\parallel + \sigma_\perp$) has been used to discriminate (in-situ and in remote sensing) between ice crystals and water droplets (e.g., Nichman et al., 2016; Mahrt et al., 2019; Zenker et al., 2017). On the other hand, r_{pol} also changes with refractive index (Fig. 2e) and has therefore been used to, e.g., differentiate between different dust particles (Glen and Brooks, 2013, 2014). However, r_{pol}'s response to the refractive index is not as linear as the ratio between the σ_F and σ_B (Fig. 2d and 3d) which has also been used to discriminate between particles of different composition over size (Glen and Brooks, 2013, 2014; Baumgardner et al., 1996). It is defined as:

https://doi.org/10.5194/egusphere-2026-3790
Preprint. Discussion started: 6 August 2026

$$r_{\mathrm{F/B}} = \frac{\sigma_F}{\sigma_B}. \tag{2}$$

To derive the scattering cross sections needed for equations (1) and (2), the intensities measured by the instruments must be multiplied by a scale factor unique to each detector (to convert from the units of digital counts to cm^2), defined as:

$$\sigma_i = c_i \cdot I_i, \tag{3}$$

where i denotes the forward (F), perpendicular ($\perp$), or parallel channel ($\parallel$) of the measured intensity I_i, while c_i represents the instrument-specific scale factor to derive the respective σ_i; with more details in Sect. 2.2 and 4.1. The parameters of r_{pol} and $r_{\mathrm{F/B}}$ can then e.g., be used to distinguish between solid and liquid particles or can serve as indicators to detect differences in refractive index.

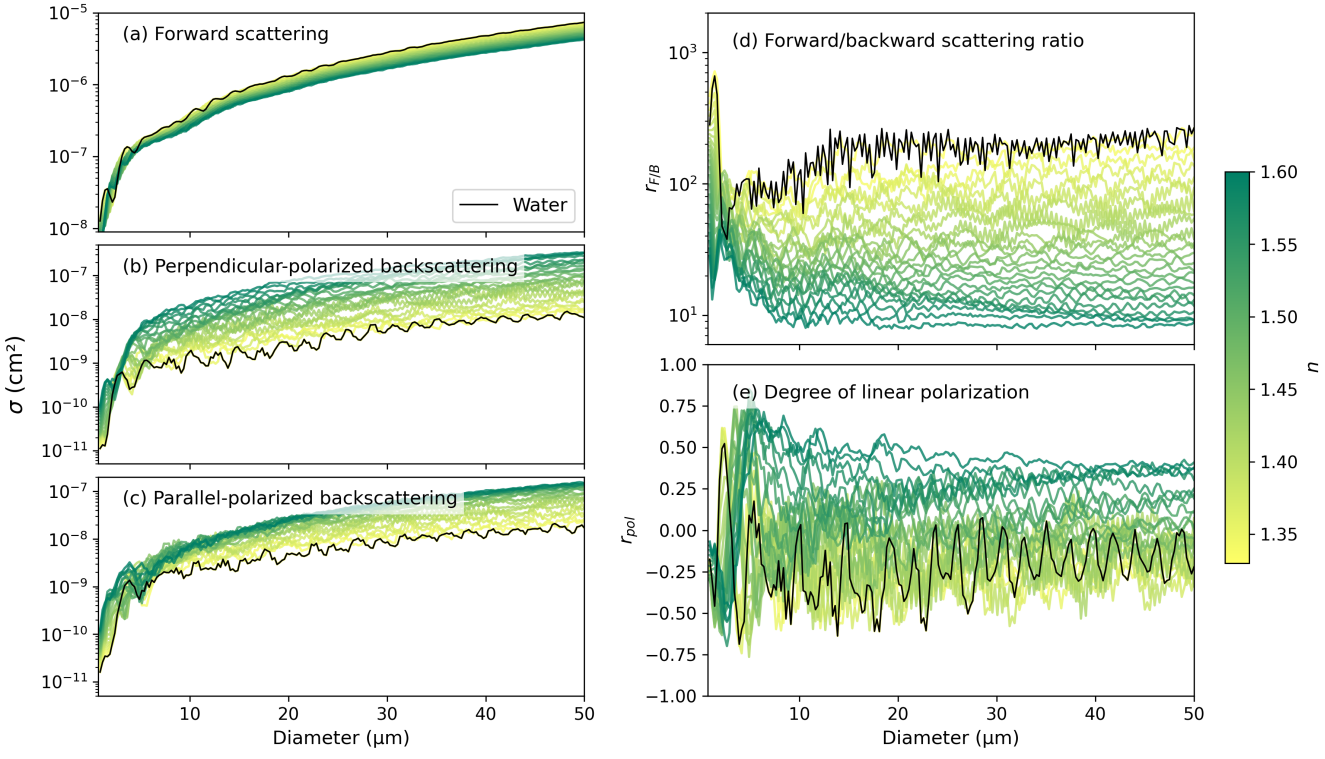

Figure 2. Modeled scattering responses of different particle diameters for the GFAS detectors. Calculated scattering cross sections σ (a-c), $r_{\mathrm{F/B}}$ (d), and r_{pol} (e) for the GFAS collection angles at refractive indices $m = n + 0i$, with n varying between 1.33 (water, black line) and 1.6.

In contrast to σ_F, the σ_B increases by over an order of magnitude with increasing refractive index, with slight differences for the perpendicular and parallel polarized components (Fig. 2b and c). The $r_{\mathrm{F/B}}$ is therefore highly sensitive to the refractive

https://doi.org/10.5194/egusphere-2026-3790
Preprint. Discussion started: 6 August 2026

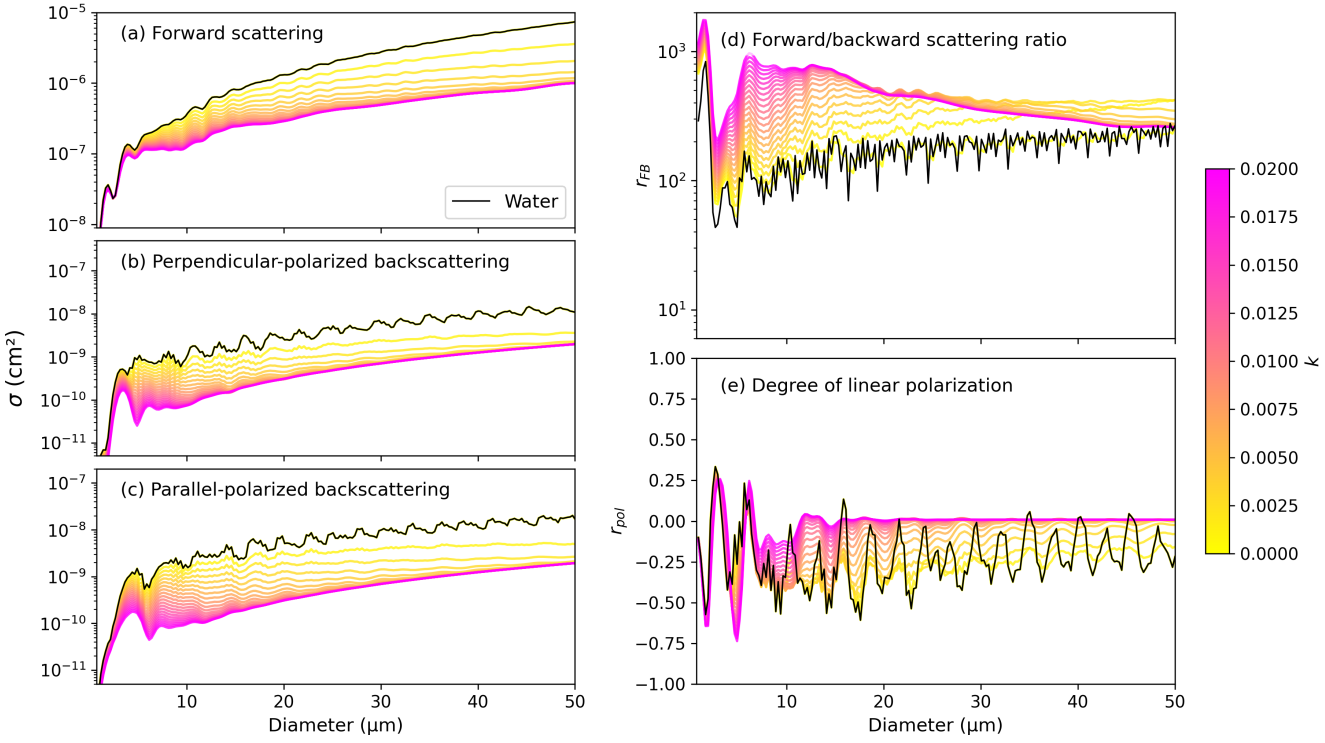

Figure 3. Same as Fig. 2 but for changing imaginary parts (k) of the complex refractive index $m = n + ki$, while the real part was set to water ($n = 1.33$, black line).

index (Fig. 2d). While lower refractive indices show a $r_{\mathrm{F/B}} > 100$ for almost the entire size range, the value decreases to around 10 for the larger refractive indices and larger particles > 10 μm. In the smaller size ranges below around 3 μm, the $r_{\mathrm{F/B}}$ shows a less pronounced and clear dependence on n compared to the larger particle size range. r_{pol} is less straightforward to interpret for different values of n; however, as the imaginary part increases, r_{pol} converges towards 0 for particles larger than 20 μm (see Fig. 3e). Given that the scattering of nonspherical particles is a challenge to model, the response of r_{pol} was experimentally evaluated in the laboratory (see Sect. 2.2).

4 Data processing

The GFAS provides its measurements in two different formats: (a) as single-particle data and (b) as 1-Hz binned data. Within the 1-Hz data, the particles are already counted and binned into predefined size intervals. The single-particle data, or Particle-by-Particle (PbP) data, capture the peak scattering intensity of individual particles as measured by all four detectors.

In the PbP data, each detected particle's peak forward (I_{F}) and backward polarization scattering intensities ($I_{\perp}$ and $I_{\parallel}$) are recorded in Analog to Digital Counts (ADC), which are subsequently used to estimate an equivalent optical diameter (d_{opt})

https://doi.org/10.5194/egusphere-2026-3790
Preprint. Discussion started: 6 August 2026

and to extract additional information about particle shape or refractive index if the particles can be assumed to be spherical. It is important to note that none of the GFAS data are pre-corrected for particle losses or instrument specific detector sensitivities; such corrections must be applied during post-processing to ensure data quality, which will be described in the following section.

4.1 Detector calibrations

Two calibration steps are needed to infer the correct particle size from the measured scattered light intensity: (a) a detector-specific conversion (scaling) factor (see Eq. (3)) is derived in order to convert measured intensities into σ, and (b) a theoretical relationship between σ and d_{opt} is parameterized with a strictly-monotonic function. Finding the theoretical relationship between σ and d_{opt} is straightforward. σ of water is calculated for the GFAS specific measurement setup and a polynomial function is used to find the best fit to predict d_{opt} from σ (for more details see Appendix A2). However, finding the correct scale factors for each detector is more challenging due to inherent uncertainties within the optical measurement setup, as well as the Mie-oscillations themselves.

The most common method to determine the scaling factors of the detectors in scattering spectrometers is to use monodisperse reference particles (e.g., glass beads). However, we have found that using glass beads can lead to high uncertainties in c_F (see Tab. 2 and Fig. A5). In the Appendix A, the glass bead calibration procedure is described in more detail. Additionally, finding $c_\perp$, and $c_\parallel$ for the backward-scattering detectors did not yield coherent results because the signal distributions of all bead sizes were too similar (see also supplementary information (SI) Fig. S1). Glass beads probably show responses different from theoretical expectations because the r_{pol} is highly sensitive to non-sphericity and surface roughness (Farias et al., 1994). We have therefore developed three alternative methods to find the scale factors using pure water spray (see Fig. 4). We call these new methods "autocalibration methods I-III" because they use water, i.e., the same medium that the instrument is designed to primarily measure. Furthermore, to better constrain the backward detectors, we developed and tested two additional techniques. Glass bead calibration will be used as a well-established reference method for the forward detector to derive the scale factor c_F, albeit with the aforementioned uncertainties. In the following, we will describe the bead calibration and introduce the three new approaches (see Fig. 4).

Standard method: Glass bead calibration

Calibrating an optical particle counter with glass beads is, in theory, fairly straightforward. Monodisperse glass beads of a known size and refractive index are measured, and each size is expected to produce a fairly narrow intensity distribution from which either the mode or the median can be assumed to be representative of the signal intensity of the nominal diameter. The σ (for glass) is calculated for the selected diameter, and c is calculated using Eq. (3).

The measured signal intensity spectrum for each glass bead size was found to be fairly broad, sometimes ranging over two orders of magnitude, and approximately log-normally distributed (see Fig. A4a). One reason for this could be that the reference particles are not strictly monodisperse but have a finite standard deviation, typically around $\pm 10\%$. When simulating the signal response of these distributions, assuming a standard deviation of 10 % for each size distribution, we found that the signal is usually non-normally distributed and shows many peaks and valleys (see Fig. A4b). When propagating the uncertainties of

https://doi.org/10.5194/egusphere-2026-3790
Preprint. Discussion started: 6 August 2026

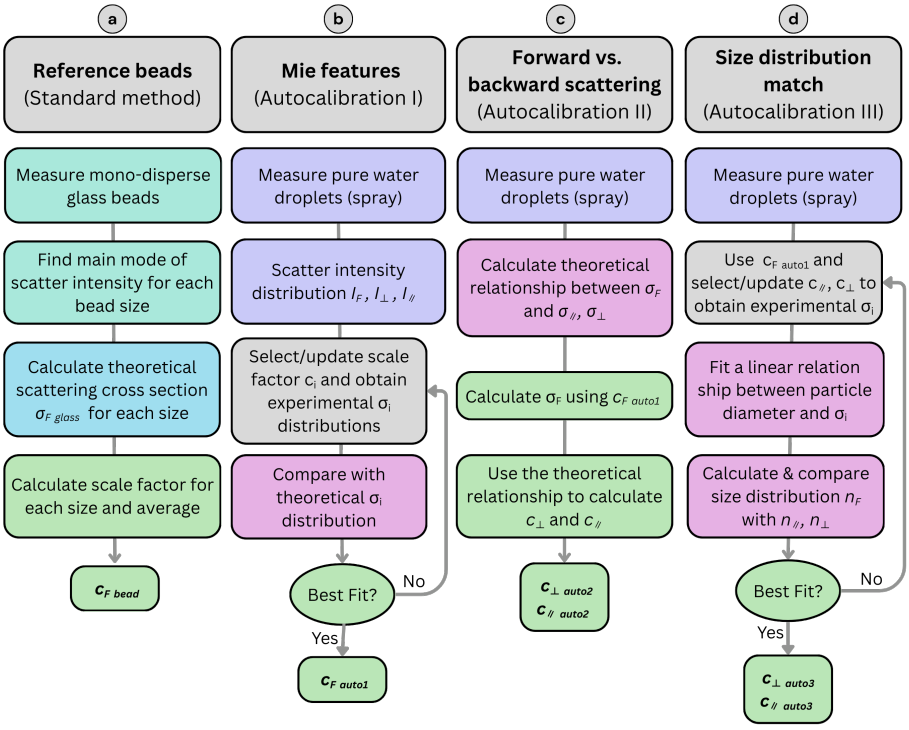

Figure 4. The different calibration methods for deriving the instrument-specific scale factor c to convert measured scattering intensities into scattering cross sections. Method a is a standard method for cloud probe calibration, while methods b-d have been developed within this work (see text for details). Further detailed flow diagrams for method b and d are shown in Fig. S2 and S3. Colors indicate connected parts within the methodology. Turquoise: glass bead measurements, violet: water measurements, light blue: modeling glass bead measurement response, pink: modeling water measurement response, green: final step, statistics and results, gray: iterate scale factors.

both distributions, the measured and modeled, the scale factor derived for the different glass bead sizes does not only have a rather large standard deviation but also increases with bead size (Fig. A5). More details on glass bead derived scale factors can be found in Appendix A3. Instrument specific uncertainties and the inherent oscillations in the Mie scattering response additionally introduce a size-dependent error in the signal intensity of between 16 and 102 % for particles smaller than 12 μm which is difficult to model for each particle size (see Appendix C). We therefore decided to only use the 15 and 30 μm glass beads for our final scale factor. The error propagation and description of the uncertainties related to the measurement setup can be found in the Appendix C.

https://doi.org/10.5194/egusphere-2026-3790
Preprint. Discussion started: 6 August 2026

Autocalibration I: Mie features matching

The first autocalibration method uses the intrinsic Mie oscillations to derive the scale factor (see Fig. 4b). As mentioned in Sect. 3, the relationship between σ and particle diameter is not linear, and several diameters lead to the same σ. This means that these σ will be sampled with a higher probability than others. As a result, a naturally smooth size distribution will have artificial but reproducible bumps and valleys. These bumps and valleys can be modeled by calculating σ for the GFAS specifications and comparing the frequency distribution of the modeled σ with the frequency distribution of the I of measured pure water droplets. To compare the two frequency distributions, an initial scale factor has to be assumed to translate I to σ. Then, the correlation coefficient r and a χ^2-test are calculated to evaluate the similarity of the two distributions. In an iterative process, the scale factor is changed until an optimum fit is found(see Tab. 2). In order to capture the features in the measured droplet distribution that correspond to the Mie oscillations, the width of the bins is set to 500 ADC per interval, and the comparisons are restricted to bins that have at least 10 and no more than 100 droplets in them.

Autocalibration II: Forward-to-backward adjustment

To constrain $c_\perp$ and $c_\parallel$, the autocalibration II uses the linear relationship (in log-log space) between σ_F and $\sigma_\perp$ or $\sigma_\parallel$ (see Fig. S4c):

$$\log_{10}(\sigma_i) = a_i \cdot \log_{10}(\sigma_F) + b_i \tag{4}$$

Where i denotes the parallel ($\parallel$) or perpendicular ($\perp$) polarization. If we use c_F from either the bead calibrations or the Mie-oscillation-matching, and the slope a and intercept b from Eq. (4), σ_i can be replaced by $c_i \cdot I_i$ (see Eq. (3)), and the equation can be solved for c_i (see Fig. 4c):

$$c_i = 10^{a_i \cdot \log_{10}(c_F I_F) + b_i - \log_{10}(I_i)} \tag{5}$$

With this approach, $c_\parallel$ and $c_\perp$ can be calculated for each droplet of measured pure water, from which we obtain a frequency distribution of possible c. We found that the geometric mean of $c_\parallel$ and $c_\perp$ yields the best resulting r_{pol} and $r_{\mathrm{F/B}}$ compared to theoretical calculations (not shown).

Autocalibration III: Size distribution match

The third method, developed to find $c_\perp$ and $c_\parallel$, is to match the calculated size distributions derived from all detectors separately (see Fig. 4d). This procedure is similar to Method I, but instead of looking at a small part of the distribution with a smaller sample size, this method uses the entire sample period and size distribution. First, an equation for a monotonic fit between σ and diameter is found for each detector (Eq. (A3)). For the forward detector, the c_F has already been established by autocalibration I, and particle size can be directly calculated. For the back-scattering detectors, a range of scale factors for $c_\parallel$ and $c_\perp$ is assumed to translate measured I into σ. Then, using these scale factors and the equations from the monotonic fit, the particle size distributions are calculated. These size distributions can then be compared to the forward size distribution via, e.g., the

https://doi.org/10.5194/egusphere-2026-3790
Preprint. Discussion started: 6 August 2026

Kolmogorov Smirnov (K-S) test. The size distribution that fits best to the forward size distribution will contain the best estimate for $c_\perp$ and $c_\parallel$.

Table 2. Scale factors for converting the GFAS signal Intensities I to scattering cross sections (cm^2) for the three different detectors. The values are provided as geometric mean (s_{geo}), median [25 %, 75 % quartiles], or arithmetic mean ± std, dependent on the applied statistics. The final scaling factors for the backward detectors is the average between autocalibration method II and III. The values for $c_\parallel$ and $c_\perp$ of autocalibration I are marked with an asterisk (*) because they are not being considered to be well constrained.

Method	F detector (c_F)	Perpendicular detector ($c_\perp$)	Parallel detector ($c_\parallel$)
Glass beads $(15.0 \pm 1.5)\,\mu$m	3.39 (1.38)	-	-
Glass beads $(30.0 \pm 3.0)\,\mu$m	4.08 (1.42)	-	-
Autocalibration I	4.17 ± 1.18	-	-
Autocalibration II	-	$1.94[1.39, 2.59]$	$0.55[0.39, 0.80]$
Autocalibration III	-	2.06 ± 0.2	0.64 ± 0.03
Final scaling values	4.17	1.99	0.59

4.2 Correcting for sampling losses

Reliable observational data requires systematic correction for both sampling and transport losses within the GFAS inlet. To correct for these effects, the approach developed by Spiegel et al. (2012) for the FM-100 was adopted for the GFAS specifications (see Fig. 1 and Tab. 1). Particles in moving air will generally follow the streamlines; however, due to their inertia, if these streamlines bend, larger particle trajectories will no longer follow those of the air. When particles are being sampled with a system that uses a blower to draw the particle-laden air through an inlet, some particles may impact the wall of the inlet if the air approaches the inlet from an angle. If the sampled particles are being carried by the ambient wind, then these losses can be exacerbated if the wind direction is not aligned with the inlet's orientation. With an increase in the difference between wind direction and sampling orientation, sampling losses increase (unless the wind speed is very low) especially for large particles. For angles larger than 90 °, however, the majority of sampling losses can no longer be calculated (Spiegel et al., 2012). To mitigate these losses, the GFAS was designed to actively align horizontally with the wind direction. However, even under ideal isoaxial conditions where wind and inlet orientations are aligned, sampling losses cannot be neglected due to wall impaction, turbulent deposition, and sedimentation within the inlet (Spiegel et al., 2012). In addition, the automated wind alignment of the GFAS inlet is not continuous due to the turbulent nature of the wind. Substantial sampling losses can therefore still occur even when orientation and wind direction do align. The sampling loss corrections also do not take vertical wind into consideration, so strong updrafts can additionally decrease sampling efficiency that cannot be accounted for when only using the horizontally measured wind direction recorded by the GFAS. The consideration of particle sampling losses is particularly relevant for a reliable determination of the liquid water content (LWC), which is dominated by larger droplets. The correction for sampling losses was applied to the GFAS in-situ measurements of this work. An overview of applied corrections is found in Fig. S5 in SI.

https://doi.org/10.5194/egusphere-2026-3790
Preprint. Discussion started: 6 August 2026

5 Results and discussion

5.1 Ambient observations at Sonnblick Observatory

Two contrasting events were selected exemplarily to showcase ambient measurements taken by the GFAS at SBO: one (liquid) cloud event (August 11-12, 2024) and one dust event (August 16, 2024). The cloud event started around 18:00 on August 11, when visibility slowly decreased, then stayed low (below 100 m) and remained fairly constant for several hours (see Fig. 5d). After midnight, the cloud started to decrease in density until around 02:00. The time span in which the visibility stayed constantly below 100 m (21:36-00:35) will be called the dense cloud period and will be used for evaluating the polarization signals in later sections (see hashed period in Fig. 5). With the visibility decreasing, N (particles > 1 μm) increases in the GFAS up to values between $500 - 700\,\mathrm{cm}^{-3}$. Around 22:00, N decreases towards $200\,\mathrm{cm}^{-3}$ but increases shortly after and then stays constant around $500\,\mathrm{cm}^{-3}$ for the rest of the dense cloud period. After the dense cloud period, N first decreases for roughly an hour, and then increases for a brief period between 01:00 and 02:00, after which the cloud fully disappears. While N increases relatively quickly at the beginning, the LWC measured by the GFAS increases slowly towards a maximum of around 0.3 $\mathrm{g\,m}^{-3}$ (when loss corrected) at around 21:30, indicating smaller droplets at the beginning of the cloud event (Fig. 5c). LWC then slowly decreases throughout the dense cloud period and only increases again between 01:00 and 02:00, simultaneous with the decrease in N. D_{eff} increases almost step-wise from 3 μm (cloud free) to around 5, 7, and then 11 μm at the beginning of the dense cloud period. Similarly to LWC and N, D_{eff} also decreases throughout the dense cloud period and shows another peak between 01:00-02:00. Loss corrections, which impact larger droplets more than smaller ones, influence LWC and D_{eff} more than N (see difference in the hashed vs. continuous black lines in Fig. 5a vs. b and c). The larger losses in the beginning of the event can be attributed to the difference between wind direction and GFAS orientation (the sample angle) as well as the availability for different efficiency corrections (see also Sect. B and Fig. S5g and h). Certain sample efficiencies can only be calculated under specific wind speed and sample angle conditions and outside of that range, these efficiencies cannot be considered and are therefore not available. In this case, the total losses calculated seem to be lower than expected because not all of the loss corrections can be applied all the time through the cloud event. The GFAS consistently reported significantly higher N than the FM (500 vs. $150\,\mathrm{cm}^{-3}$). However, the LWC of GFAS and FM are remarkably similar (excluding a dip in LWC for the GFAS roughly around 22:00). The PVM follows the same temporal trends as both droplet spectrometers but measures a higher LWC than both the FM and GFAS during the dense cloud period. An opposite effect is observed for the D_{eff}, where the PVM measures the lowest values and the FM is highest, with the GFAS in between. With a higher N but similar LWC and smaller D_{eff}, the GFAS clearly measures more and smaller droplets compared to the FM (see also the size distribution in the SI Fig. S6).

Throughout the cloud event, the r_{pol} shows a decrease in values for larger particles, which is expected for spherical particles with a refractive index close to water (see Fig. 2e). However, according to the theory, r_{pol} should approach negative values consistently for particles larger than 6 μm, whereas in this cloud case, the r_{pol} is predominantly negative for particles only larger than 15 μm. r_{pol} seems to be higher than expected over the entire size range. We assume that the refractive index of cloud droplets is higher than that of pure water since they contain (partially) dissolved aerosol (Cotterell et al., 2017). Interestingly,

https://doi.org/10.5194/egusphere-2026-3790
Preprint. Discussion started: 6 August 2026

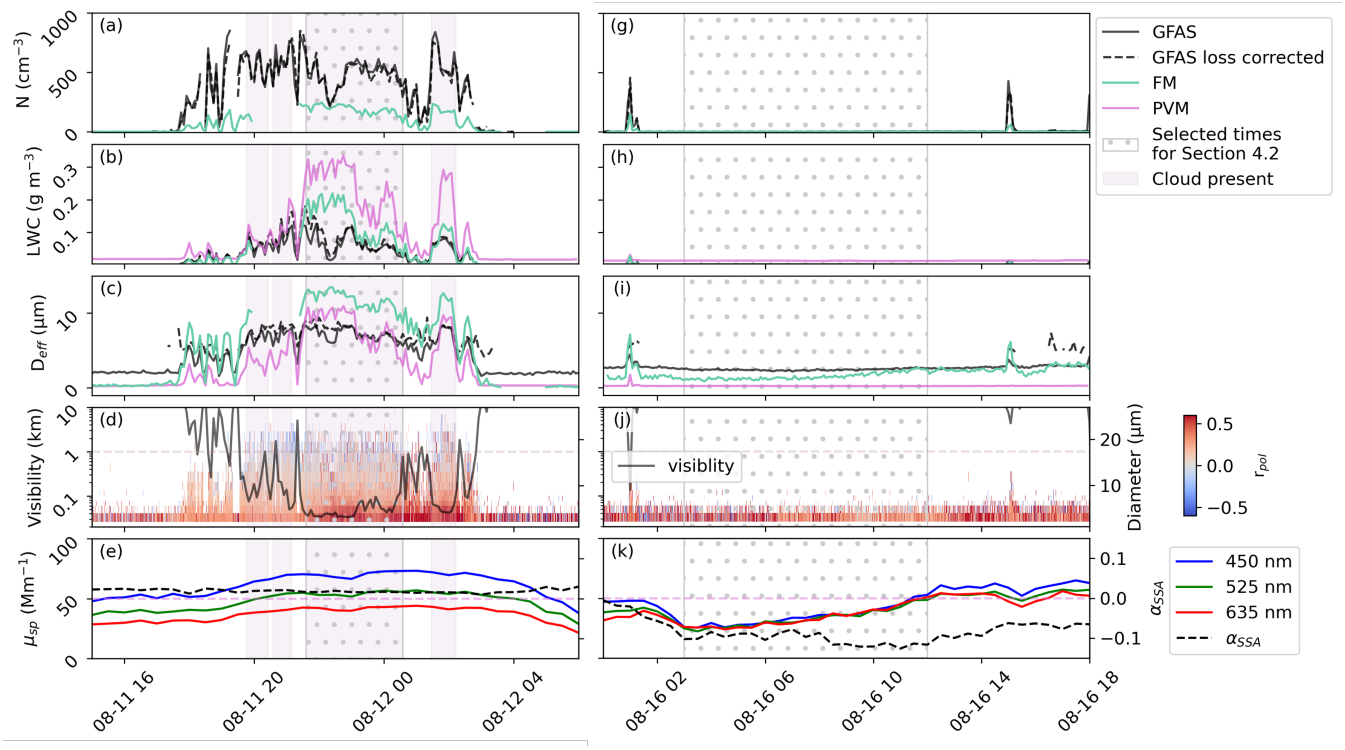

Figure 5. Example cloud event on August 11-12 2024 (a)-(e) and Saharan dust event on August 16 2024 (g)-(k). Number concentration N (a, g), Liquid Water Content LWC (b, h), effective Diameter D_{eff} (c, i) of the GFAS (black), the Fog Monitor (FM, green) and PVM (purple), GFAS degree if linear polarization r_{pol} per particle size and visibility < 10 km (d, j), particle light scattering coefficient μ_{sp} for three different wavelengths (blue, green and red) and single scattering albedo ångström exponent (α_{SSA}, black dashed line) (e, k) measured at Sonnblick Observatory (SBO).

r_{pol} changes over time, especially for smaller particle sizes. Although initially the values for small particles <10 μm showed values around 0.25, r_{pol} increases for that size range in the middle of the dense cloud period and then fluctuates over time. In the hours around and during the cloud event, the μ_{sp}, as well as α_{SSA}, measured in parallel at the SBO observatory, stayed relatively consistent, suggesting that aerosol properties did not change significantly throughout these hours (see Fig. 5e). A change in the underlying overall aerosol properties is therefore not likely to be the reason for the change in r_{pol} but rather a change in cloud microphysical properties.

An SDE is observed at SBO starting on August 16 and lasting until August 18. Within that period, a shorter interval is chosen, where α_{SSA} seems fairly stable and low (around -0.1), indicating the prevalence of mineral dust, while the μ_{sp} shows almost the same values for all three wavelengths, suggesting a coarse particle mode in which the GFAS is able to measure particles (hashed period, see Fig. 5). This event (lasting from 03:00 to 12:00 on August 16) will be analyzed further in Sect. 5.2 and will, from here on, be called the dust event. During the dust event, the GFAS measures an average number concentration of 1 cm^{-3}. The majority of particles are below 5 μm with few particles larger than 10 μm. The LWC is below 10^{-7} g m^{-3} for

https://doi.org/10.5194/egusphere-2026-3790
Preprint. Discussion started: 6 August 2026

both FM and GFAS, while the PVM shows a common offset for cloud free periods. The r_{pol} varies throughout the dust event, first with values around 0.6 until roughly 06:00 UTC where the values decrease to around 0.2. After the dust event, around 13:00 UTC, r_{pol} increases again (see Fig. 5j).

5.2 Distinguishing spherical from nonspherical particles

To understand the response of the GFAS to different types of particles, we measured a variety of substances in the laboratory. The r_{pol} shows a clear difference in the size-dependence of the liquid water and solid particles for the selected compounds (Fig. 6). These differences in r_{pol} start to show at around 7 μm, where the average r_{pol} for nonspherical particles significantly deviates from that of water droplets. For water droplets, the median r_{pol} and its inter-quartile range decreased with particle d_{opt}, approaching -0.4 for the largest sizes.

For nonspherical and solid particles, including cellulose and volcanic dust, the r_{pol} displayed greater variability and minimal trends with increasing d_{opt}, fluctuating around 0.4, with a slight dip towards smaller values between $15-20\,\mu$m. We assume that r_{pol} does not show a trend with increasing size for nonspherical particles due to their varying shapes and orientations as they pass through the laser beam, along with possible absorbance. The fact that there is no obvious size dependency in r_{pol} of nonspherical particles is somewhat contrary to the findings of Glen and Brooks (2013), who observed a clear change in polarization with increasing size for different types of mineral dust. However, in a later paper of theirs, this trend in polarization over d_{opt} was much lower or had totally disappeared (Glen and Brooks, 2014). One reason for the differences in their findings could be that in the later publication, Glen and Brooks (2014) measured with an upgraded version of the CASPOL, where the backward scattering setup was changed. In Glen and Brooks (2013), the polarization ratio $\delta = I_{\parallel}/I_B$ was used as a measure of changes in polarization, whereas in Glen and Brooks (2014), the depolarization ratio $DR = I_{\perp}/I_{\parallel}$ was taken. Furthermore, it also seemed that the derived signal intensities in both publications were not calibrated to σ; therefore, the measurements could lead to different results in the two versions of the CASPOL.

For sizes larger than 5 μm, glass bead r_{pol} is higher than for water, which is expected for higher refractive indices in that size range. Interestingly, however, glass beads show a slight decrease of r_{pol} with particle size, even though they were meant to be monodisperse at 15 μm. Since they have a higher refractive index than water, it is reasonable that they are sized smaller (see also Sect. 3), but they appear in a fairly broad size range below 10 μm. As discussed in Sect. 4.1, glass bead measurements can be accompanied by large uncertainties, partially due to Mie oscillations. However, we also observed that they do not behave as predicted by the theory in the backward scattering collection angles (Appendix 4.1).

In Fig. 6, the average size-dependent r_{pol} for the cloud and dust event observed at SBO is shown. The cloud event at SBO (hashed period in Fig. 5) showed a similar decrease of r_{pol} over particle size as the laboratory measurements of pure water droplets, however, the values were generally slightly higher and converged towards -0.15 instead of -0.35 as observed for pure water droplets in the laboratory measurements (see Fig. 6). The most likely physical explanation for the elevated values of r_{pol}, as mentioned earlier, is that the measured cloud water at SBO has a different refractive index than pure deionized water. Dissolved or insoluble material within cloud droplets can increase both the real (scattering) and the imaginary (absorbing) parts of the refractive index (Baumgardner et al., 1996; Shepherd et al., 2018), changing its optical properties and therefore its r_{pol}

https://doi.org/10.5194/egusphere-2026-3790
Preprint. Discussion started: 6 August 2026

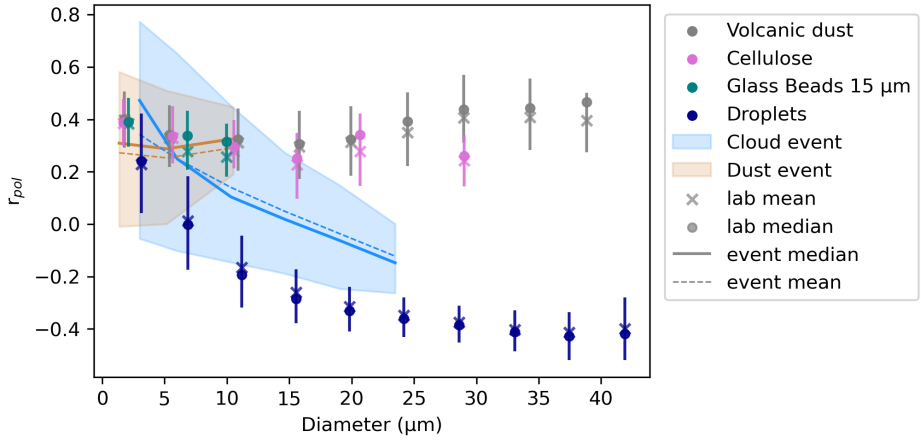

Figure 6. Degree of linear polarization r_{pol} of different aerosol types and droplets over the optical diameter d_{opt} measured in laboratory and in the field. Laboratory measurements of r_{pol} for various test aerosol and water droplets are shown as markers (error bars: 25$^{\mathrm{th}}$ and 75$^{\mathrm{th}}$ quartiles), while in-situ measurements at Sonnblick Observatory (SBO) are shown as lines (median and mean values, shaded areas show 25$^{\mathrm{th}}$ and 75$^{\mathrm{th}}$ quartiles).

(see also Fig. 2). The large interquartile range of r_{pol} over diameter (25-75%, shaded area in Fig. 6) across all particle sizes also supports some heterogeneity in composition or refractive index in the measured droplets. Figure 6 also shows that the dust event observed at SBO exhibited a similar r_{pol} (around 0.3) to the nonspherical particles probed in the laboratory experiments. While the median r_{pol} is initially slightly smaller than that for the substances measured in the laboratory experiments and the cloud event, it increases somewhat for particles >5 μm towards 0.35. It is important to note here that we measured significantly fewer particles during the dust event than for most other laboratory substances displayed here, especially above 5 μm.

Looking at $r_{\mathrm{F/B}}$ (Fig. 7), the laboratory measurements of water droplets show a clear size dependence in their frequency distribution, which appears approximately log-normally distributed and shifts toward higher values. The increase in $r_{\mathrm{F/B}}$ with larger particles seems to be in line with the calculations done in Sect. 3. The cloud event exhibits a broadly similar behavior; however, $r_{\mathrm{F/B}}$ values are nearly an order of magnitude lower for small particles and display a bimodal structure in the frequency distribution for the smallest size range. The lower values of $r_{\mathrm{F/B}}$, especially for the smaller sizes, potentially indicate particles with a higher refractive index (see Fig. 2), while the bimodality across all size ranges reflects the underlying ambient size distribution. In contrast, volcanic dust measured in the laboratory follows a similar frequency distribution of $r_{\mathrm{F/B}}$ to water droplets for particles smaller than 5 μm, but deviates significantly at larger sizes. The distributions are less smooth, likely due to lower particle counts, and show a weaker size dependence overall. Notably, particles larger than 14 μm exhibit $r_{\mathrm{F/B}}$ values comparable to the smallest size range, whereas particles between 3–9 μm tend to show higher values. The ambient dust event reveals a qualitatively similar pattern across size ranges as the volcanic dust but with $r_{\mathrm{F/B}}$ values reduced by approximately half an order of magnitude. Additionally, particles larger than 9 μm are not represented due to insufficient sampling statistics.

https://doi.org/10.5194/egusphere-2026-3790
Preprint. Discussion started: 6 August 2026

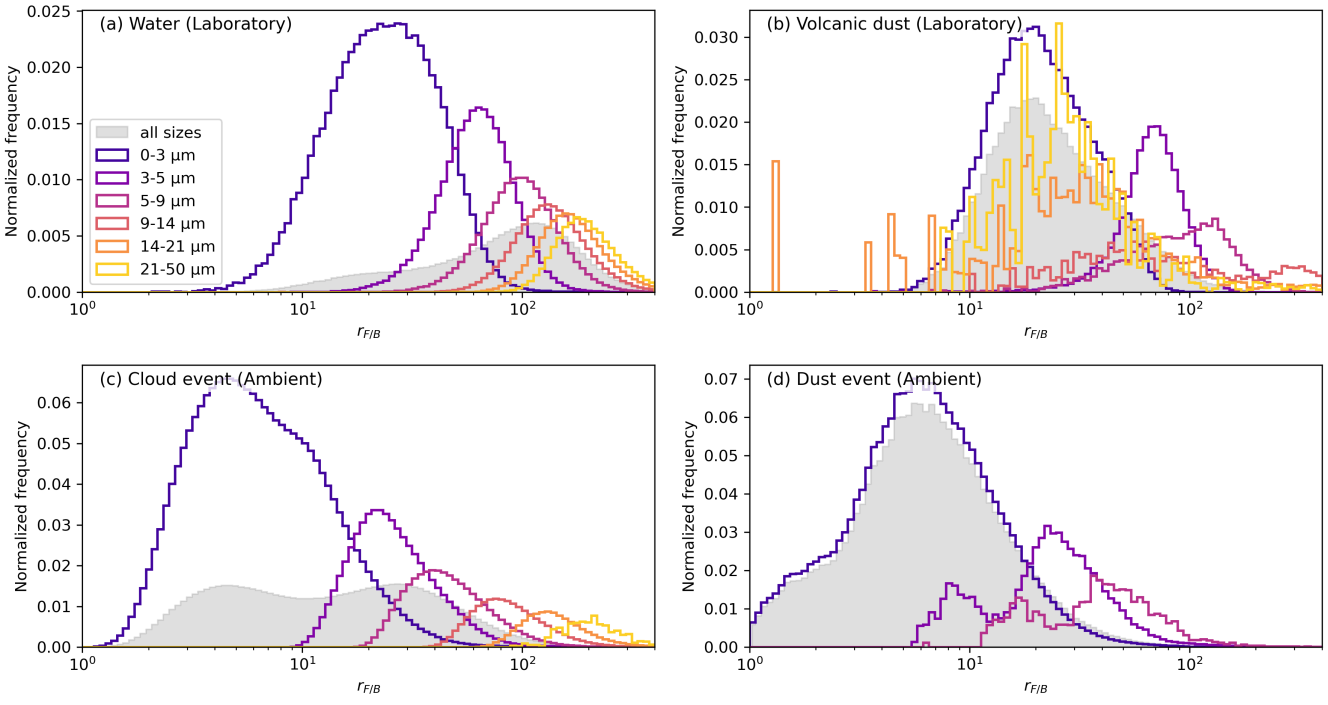

Figure 7. Size resolved frequency distribution of the forward-to-backward scattering ratio $r_{\mathrm{F/B}}$. All distributions are normalized by bin width and sample size. The gray shaded area is the frequency distribution of the full size range while the different colors describe the distribution for each size category.

The laboratory measurements of water droplets also show a clear size dependence in r_{pol} (see Fig. 8). Smaller particles (<3 μm) exhibit higher values and broader frequency distributions, with a mode around 0.35, whereas larger particles (>21 μm) show lower values and a narrow distribution, converging toward a mode near $\breve{}0.4$. In contrast, the frequency distribution of r_{pol} of the cloud event displays a more complex, multi-modal structure. For the smallest particles (<3 μm), a tri-modal distribution is observed, with modes around 0.85, -0.1, and $\breve{}0.8$. With increasing particle size, the high-value mode at around 0.8 decreases in frequency and shifts slightly to lower values but persists up to sizes of $14-21$ μm. Meanwhile, the lower mode that is around 0 for the smallest particles becomes more prominent and shifts somewhat toward more negative values, reaching approximately $\breve{}0.1$ for particles >21 μm. In contrast to both water and cloud observations, laboratory measurements of volcanic dust show almost no size dependence. The distributions remain centered around a mode of approximately 0.4 across all size ranges, with only a slight skew toward smaller values for larger particles. The SDE exhibits a tri-modal distribution similar to the cloud case, with modes around 0.95, 0.45, and $\breve{}0.8$, but shows minimal variation with particle size.

Combining r_{pol} and $r_{\mathrm{F/B}}$ can be used as a fingerprint to differentiate aerosol types and potentially cloud phases (Glen and Brooks, 2013, 2014). Figure 9 shows these frequency distributions for the laboratory measurements of water and volcanic dust, as well as the cloud and dust event measured at SBO. Contour lines show the distribution of values from different size bins

https://doi.org/10.5194/egusphere-2026-3790
Preprint. Discussion started: 6 August 2026

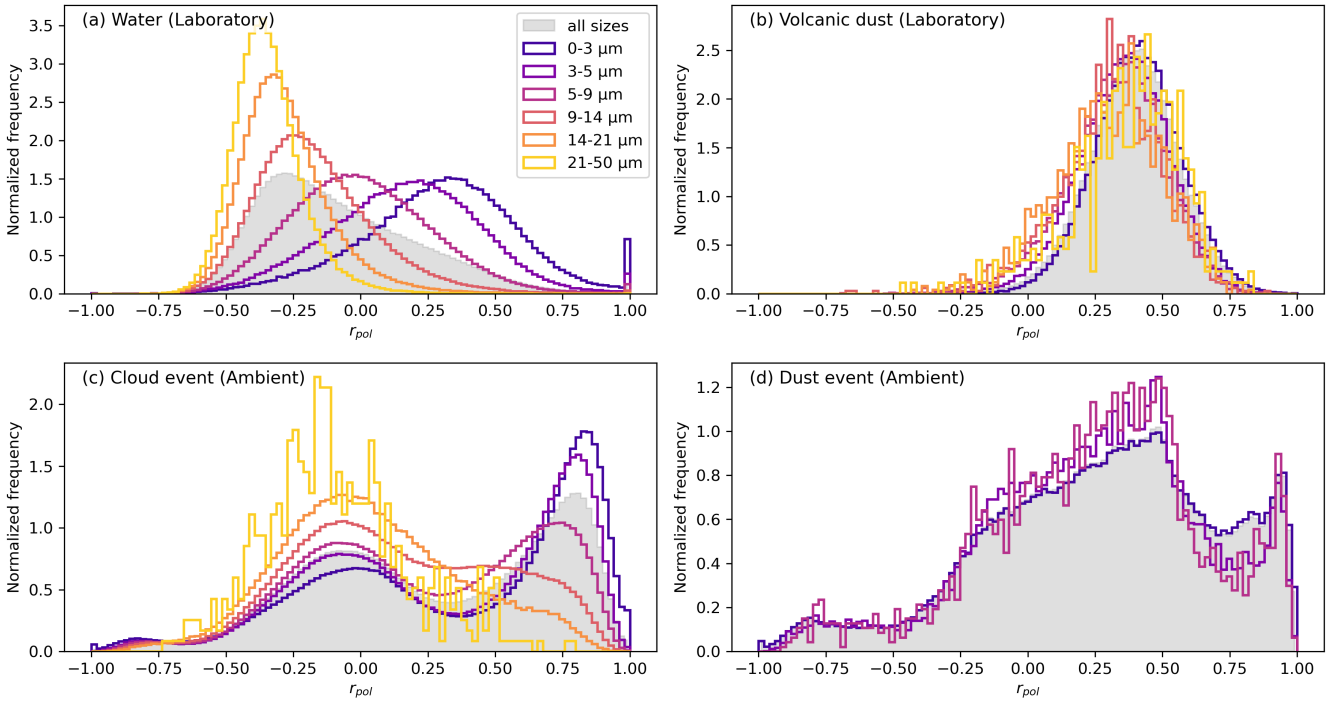

Figure 8. Size resolved frequency distribution of the degree of linear polarization r_{pol}. The gray shaded area is the frequency distribution of the full size range while the different colors describe the distribution for each size category. All distributions are normalized by bin width and sample size.

(here showing 86 % of the data to guide the reader's eye). $r_{\mathrm{F/B}}$ is increasing with particle size for all four selected examples, differing only in magnitude. Noticeably, the $r_{\mathrm{F/B}}$ for the laboratory water is seen to be higher, with a mode larger than 100, while the modes of the other substances are below 50. For water droplets measured under laboratory conditions, most values of $r_{\mathrm{F/B}}$ fall between 100 and 200, and for r_{pol} between -0.5 and 0, respectively (see dark gray shaded area in Fig. 9a).

The ambient cloud event observed at SBO is bi-modally distributed in both r_{pol} and $r_{\mathrm{F/B}}$ (see Fig. 9c). Only in the smallest size range can we identify the small mode also visible in Fig. 8c at $r_{\mathrm{pol}} = -0.85$. The reason for this observed bimodality in the ambient data is difficult to identify. It is unlikely that these large particles with a high r_{pol} are interstitial aerosol since they exist in size ranges even larger than 14 μm, whereas the dust event barely showed any particles larger than 9 μm. As mentioned before, we hypothesize that the cloud water composition is significantly different from pure water, which could impact the droplet's optical properties. A potential increase in the droplet's refractive index would also mean that it is being undersized by scattering spectrometers, leading to an underestimation of the LWC and D_{eff}.

The $r_{\mathrm{F/B}}$-r_{pol}-relationship of volcanic dust shows a distinctly different pattern compared to water droplets (see Fig. 9a and b). As discussed before, r_{pol} of dust is clearly higher due to the nonspherical nature of the particles and a higher refractive index. As expected, given that the properties of Saharan and volcanic dust are quite different due to their vastly different origins,

https://doi.org/10.5194/egusphere-2026-3790
Preprint. Discussion started: 6 August 2026

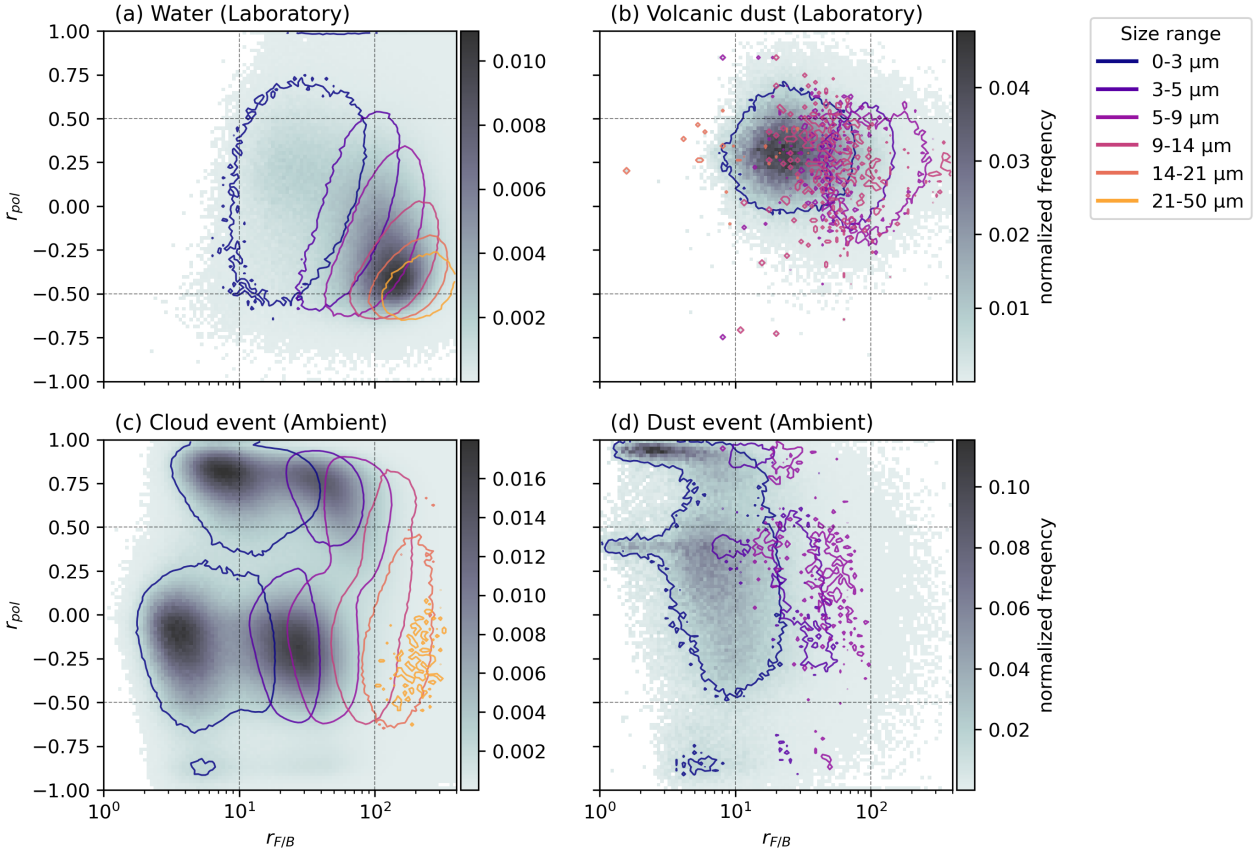

Figure 9. Frequency distributions of the degree of linear polarization r_{pol} vs. forward-to-backward ratio $r_{\mathrm{F/B}}$. Laboratory measurements of (a) water droplets and (b) volcanic dust. Measurements from the campaign at Mt. Sonnblick Observatory (SBO) during (c) a cloud event and (d) a dust event (see Fig. 5).

their $r_{\mathrm{F/B}}$ and r_{pol} patterns also differ (Glen and Brooks, 2013). The mode of r_{pol} around 0.4 in both samples (see also Fig. 8b and d) indicates some similarities in optical behavior with the volcanic dust.

The most striking difference between laboratory and ambient data is the multi-modality of the r_{pol}, which is only observed in the ambient data (see Fig. 9 and 8). The bimodality as a function of the forward-to-backward ratio is even further enhanced in the cloud case. Although we cannot fully explain the observed features, the overall direction of higher size-independent polarization ratios in the SDE compared to the cloud event is in line with the laboratory experiments.

5.3 Recommendations

For the retrieval of reliable aerosol and cloud microphysical parameters from measurements with the GFAS, and for future work and developments, we can make the following recommendations:

https://doi.org/10.5194/egusphere-2026-3790
Preprint. Discussion started: 6 August 2026

1. For the standard glass bead calibration of the forward scattering detector, we recommend using several glass bead sizes, especially diameters above 12 μm to reduce the errors induced by Mie-oscillations.

2. To ensure proper simultaneous calibration of all three detectors, a water droplet calibration using the autocalibration methods presented here should be applied. This is crucial to ensure compatibility between different observations and different instrumentation.

3. To ensure that all detectors are properly calibrated and the optical alignment is in place before deployment, we further recommend that frequency distribution plots of the $r_{\mathrm{F/B}}$ signal, as well as for the r_{pol} (see Fig. 7 and 8), be done early on with nebulized pure water. Within the frequency distribution plots, the signals of a properly functioning and calibrated instrument will follow a similar pattern as predicted by Mie-Lorenz theory; thus, malfunctions or calibration issues with the instrument can easily be detected.

4. Particle loss calculations with respect to sampling and transport losses should be performed to derive more accurate cloud microphysical parameters.

5. Despite many decades of advancements in cloud probe development, large uncertainties in key cloud microphysical parameters, such as LWC and N, persist among different cloud probes, as illustrated here. This calls for continuing regular and coordinated cloud probe inter-comparison exercises, as e.g. done within ECCINT ACTRIS.

6 Conclusions

Within this work, we present the new ground-based fog and aerosol spectrometer (GFAS), which is based on single-particle light scattering and polarization measurements to retrieve aerosol and cloud microphysical parameters. Since the standard glass bead calibration is prone to high uncertainties (due to the size, shape, and refractive index of the glass beads) and cannot be used to calibrate the polarized backward scattering signals, we developed a new autocalibration method based on pure water droplets and Mie-Lorenz theory. This method is easier to use than the standard method using glass beads and can be applied to all scattering spectrometers with a monochromatic light source and single-particle data. Using the new autocalibration method, we retrieve detector-specific scale factors with lower error estimates in the forward scattering. We could also derive well constrained scale factors for the backward polarized scattering signals. To our knowledge, this is the first study including the calibration of the polarized backward scattering detectors of an in-situ scattering spectrometer. This approach enables comparability across different studies with similar instruments. Furthermore, for the GFAS, we can conclude that the translation of measured optical properties to accurate microphysical parameters generally improves for larger particle diameters above around 12 μm in diameter. While sizing can have a relative error margin of up to 102% for particles smaller than 12 μm, the uncertainty decreases to 18 % for particles $> 12\,\mu$m. We performed laboratory and field measurements to characterize the signal response of the GFAS to different spherical and nonspherical particles of various compositions, as well as its performance in ambient measurement conditions. Using the degree of linear polarization (r_{pol}), nonspherical particles

https://doi.org/10.5194/egusphere-2026-3790
Preprint. Discussion started: 6 August 2026

can be well distinguished from water droplets under laboratory conditions and for particles > 7 μm. While r_{pol} for pure water decreases with optical diameter (d_{opt}) from 0.15 to roughly -0.5 over the GFAS size range, nonspherical particles do not show a significant change in polarization over size and remain roughly at values around 0.3. Ambient cloud droplets, however, show a distinctly different distribution of r_{pol} compared to the water measured in the laboratory. While the values are also decreasing over d_{opt}, they remain constantly elevated compared to pure water and are also bi-modally distributed (for droplets up to 21 μm). We hypothesize that the difference in r_{pol} between the laboratory water and ambient cloud droplets implies different refractive indices of the cloud droplets compared to pure water due to (partially) dissolved aerosol within the droplets. These properties likely influence sizing and thus, LWC, D_{eff}, and may also impact the radiative properties of the cloud.

https://doi.org/10.5194/egusphere-2026-3790
Preprint. Discussion started: 6 August 2026

Acronyms

ADC Analog to Digital Counts

APD Avalanche Photo Detector

DOF Depth Of Field

ECCINT European Center for Cloud Ambient INTer-comparison

FM Fog Monitor

FWHM Full-Width-Half-Maximum

GFAS Ground-based Fog and Aerosol Spectrometer

PbP Particle-by-Particle

PVM Particlulate Volume Monitor

RSS Root Sum Square

SBO Sonnblick Observatory

SDE Saharan Dust Event

SSA Single Scattering Albedo

Glossary

D_{eff} Effective diameter (μm)

I Scattering light intensity (ADC)

$I_{\parallel}$ Parallel polarized back-scattering light intensity (ADC)

$I_{\perp}$ Perpendicularly polarized back-scattering light intensity (ADC)

I_{F} Total forward-scattering light intensity (ADC)

LWC Liquid water content (g m^{-3})

N Number concentration (cm^{-3})

P Power of the laser (W/m^2)

P_{c} Probability of particle coincidence (%)

https://doi.org/10.5194/egusphere-2026-3790
Preprint. Discussion started: 6 August 2026

α_{SSA} Single Scattering Albedo Ångström exponent

μ_{ap} Particle Light Absorption coefficient (Mm^{-1})

μ_{sp} Particle Light Scattering coefficient (Mm^{-1})

σ Scattering cross section (cm^2)

σ_B Scattering cross section of the backward scattering angles of the GFAS (cm^2)

σ_F Scattering cross section of the forward scattering angles of the GFAS (cm^2)

$\sigma_{\parallel}$ Scattering cross section of the parallel polarized backward scattering angles of the GFAS (cm^2)

$\sigma_{\perp}$ Scattering cross section of the perpendicularly polarized backward scattering angles of the GFAS (cm^2)

θ_s Scattering efficiency

c Scale factor to scale the measured scattering intensity towards scattering cross section ($\mathrm{cm}^2/\mathrm{ADC}$)

c_F Scale factor for the forward scattering detector ($\mathrm{cm}^2/\mathrm{ADC}$)

$c_{\parallel}$ Scale factor for the backward parallel polarized detector ($\mathrm{cm}^2/\mathrm{ADC}$)

$c_{\perp}$ Scale factor for the backward perpendicularly polarized detector ($\mathrm{cm}^2/\mathrm{ADC}$)

d_{beam} Cross section of the laser beam (mm)

d_{opt} Equivalent optical diameter (μm)

$r_{\mathrm{F/B}}$ Forward-to-backward scattering ratio

r_{pol} Degree of linear polarization

s_{geo} Geometric standard deviation

https://doi.org/10.5194/egusphere-2026-3790
Preprint. Discussion started: 6 August 2026

Appendix A: Calibration techniques

In the following, we present more general details on calibrating scattering spectrometers, with a focus on the GFAS measurement setup. Although the derivation of d_{opt} from the forward scattering intensity I_{F} is straightforward, as will be explained below, there are several factors that complicate this derivation and must be recognized as sources of uncertainty in the subsequent derivation of particle size.

A1 Theoretical basis for d_{opt} extraction from light scattering measurements

The collection angles of spectrometers are determined by the geometry of the instrument. As an example, Fig. A1 illustrates what determines the forward scattering collection angles of the GFAS.

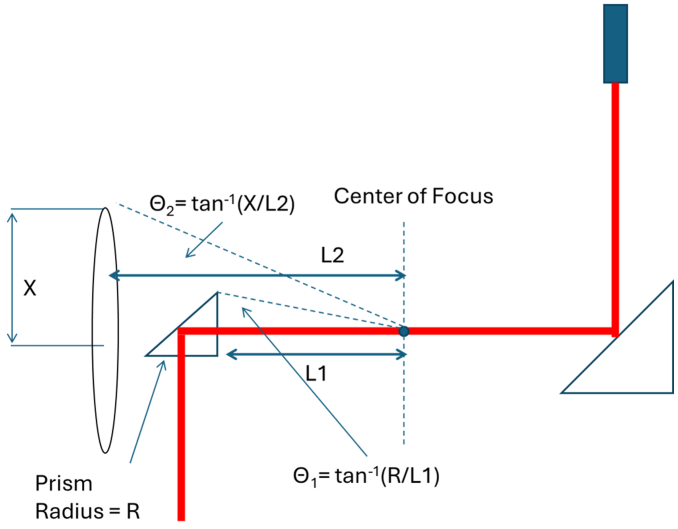

Figure A1. The optical collection angle θ_2-θ_1 in a forward scattering spectrometer. θ_1 is determined by the distance between prism and center of focus ($L1$), and the radius of the prism (R), while θ_2 is determined by the distance between the objective lens and the center of focus ($L2$).

The particle parameter determined from the Mie-Lorenz theory, which relates to the incident light, is the scattering efficiency θ_s. This is a non-dimensional measure of the fraction of the incident light that is scattered by the particle.

The scattering cross section, σ, of a particle with radius r is the product of its scattering efficiency θ_s and cross-sectional area πr^2:

$$\sigma = \theta_s \pi r^2 \tag{A1}$$

The intensity of the scattered light, I, is the product of the σ and the power, P, of the light source:

$$I = P\sigma, \tag{A2}$$

https://doi.org/10.5194/egusphere-2026-3790
Preprint. Discussion started: 6 August 2026

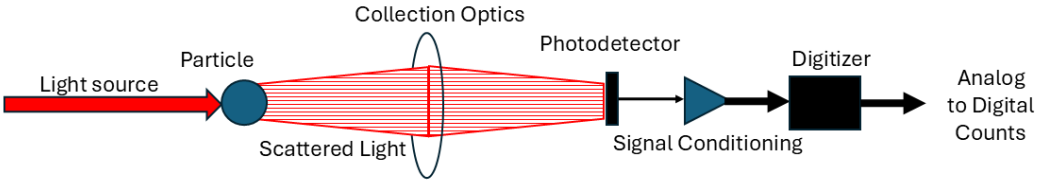

Figure A2. Basic setup employed by all the light scattering spectrometers to measure light scattered by individual particles.

where P is usually given in watts per unit area.

Figure A2 is a schematic of how the light scattering spectrometers detect the scattered light and convert it into a digital signal that can be processed to extract the particle size. A particle excited by a light source will scatter light anisotropically, i.e., in all directions but not with the same photon density. The optical system of the spectrometer collects some fraction of this light and focuses it onto a photodetector that converts the photons into a current, after which it is conditioned (filtered and amplified) before being digitized by an analog-to-digital converter.

Equations (A1) and (A2) describe the relationship between the I and the theoretical σ. Given that we are measuring I, we could directly relate this value to the theoretical cross sections if we know P, the wavelength λ, of the light source, the refractive index of the particle, the sensitivity of the photo-detector, the amplification of the signal conditioning electronics and the resolution of the digitizer. We actually do have all this information from which we could directly derive $\sigma_i = f(I_i)$, where i are the different detectors of the instrument. From the σ, we could determine the size of the particle; however, given the normal variability in laser power and photo detector sensitivity from instrument to instrument, the simpler approach for relating the I to σ is through calibration, commonly done with spherical particles of known size and refractive index, as briefly summarized in the previous section and as detailed in the following sections.

A2 Regression fitting and binning for this GFAS unit

In order to derive a size from the GFAS signal, as well as to compare the values of the degree of linear polarization r_{pol} and the forward-to-backward ratio $r_{\mathrm{F/B}}$ with the theory and other measurements, the output of the detectors of the GFAS must be related to the theoretical scattering cross section σ for the collection angles of the GFAS (see also Sect. 4.1 for the method of deriving the scale factors).

The I of different detectors can be converted into σ by multiplying them by a scale factor c (see also Eq. (3) in the main text). After transforming I values into σ, a polynomial regression equation in log-log space is used to convert the scattering cross section σ into a particle equivalent optical diameter (d_{opt}). In most cases, the forward scattering cross section σ_F is used for sizing, but a regression can be applied to all detectors:

$$d_{\mathrm{opt}} = 10^{m_0 + m_1 \log_{10}(\sigma) + m_2 \log_{10}(\sigma)^2}. \tag{A3}$$

https://doi.org/10.5194/egusphere-2026-3790
Preprint. Discussion started: 6 August 2026

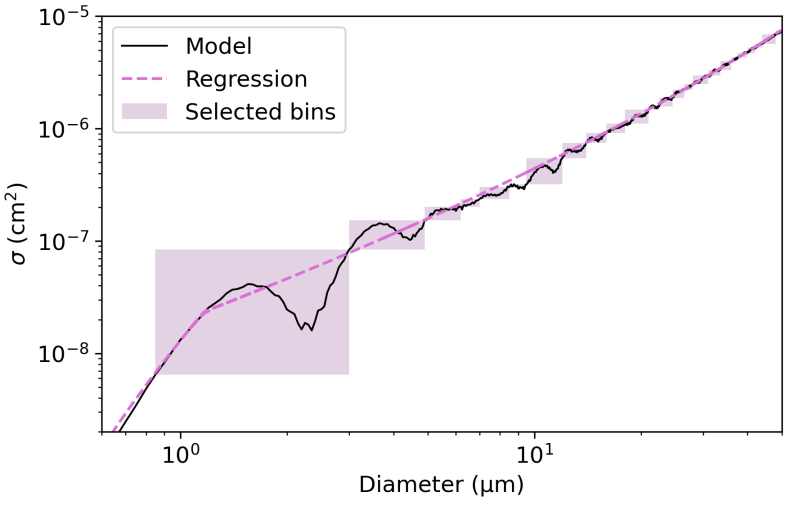

Figure A3. Selected size bins in order to account for Mie-oscillations and theoretical curve of scattering cross section (σ) of water over the GFAS size range. The shaded squares show the recommended diameter bins for the GFAS as well of the corresponding values of σ.

We found that a best fit was possible when fitting two different second degree polynomial regressions for particles smaller or larger than 1.17 μm, because around this value the slope of the theoretical curve changes strongly (see also Fig. A3). The two regressions differ in their regression coefficients m_0, m_1, m_2, which are instrument specific and listed for GFAS in Tab. A1.

Table A1. Regression coefficients of the polynomial regression equation to convert the GFAS measurement signal into equivalent optical diameter

	m_0	m_1	m_2
$D_{<1.17\mu m}$	3.544	0.644	0.025
$D_{>1.17\mu m}$	2.436	-0.196	-0.066

The fact that the theoretical relationship between particle size and σ is non-monotonically increasing and oscillating leads to the issue that we cannot differentiate between certain particle sizes because they result in the same measurement signal (see Fig. A3). For example, a particle of 2 μm has the same σ as one with a diameter of 1.1 μm. While we make use of these oscillations to auto-calibrate the GFAS, they may lead to large under-or over-sizing errors that are beyond this work to de-tangle. To avoid large errors, we binned the particle sizes into 25 Mie-oscillation-sensitive size bins (shaded boxes in Fig. A3). Table S1 in the SI shows the size bin thresholds (d_{opt}) optimized for cloud droplets, along with the corresponding σ and fitted I_F threshold values for our GFAS unit.

https://doi.org/10.5194/egusphere-2026-3790
Preprint. Discussion started: 6 August 2026

A3 Step-by-step procedure to calculate forward scattering size thresholds for glass bead calibration

In the following, we describe the different steps for finding detector specific scale factors in monochromatic light scattering spectrometers using monodisperse calibration beads. This section serves as a best practice manual for glass bead calibration.

Step 1: Measure monodisperse particles

Select and measure monodisperse, spherical calibration particles of known refractive index. A measurement with a single size is sufficient, but measuring multiple sizes decreases the uncertainty. As previously discussed, either the 1-Hz or PbP files can be processed and evaluated. Figure A4a illustrates measurements of 2, 5, 8, 15, and 30 μm crown glass beads generated from the PbP file. Use the geometric mean or the mode (fitted with a log-normal distribution) of the sampled signal distribution to continue with further calculations.

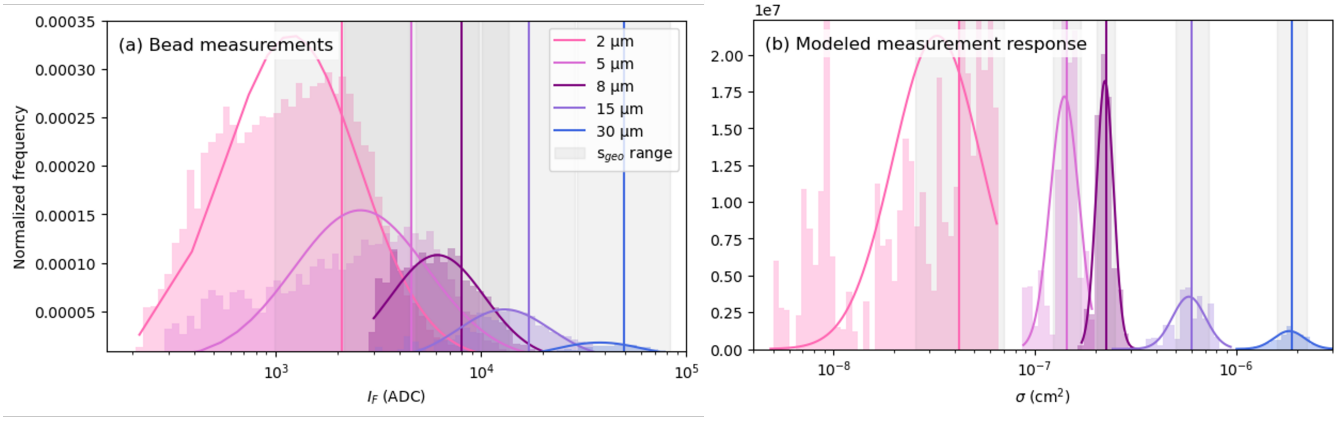

Figure A4. (a) Measured and (b) modeled response for various glass bead sizes. The derived geometric mean (vertical lines) and geometric standard deviation (s_{geo}, in gray) are shown for each measured and modeled glass bead size as well. I_{F}: Signal intensity measured in the forward detector, ADC: Analog-to-digital counts, σ: scattering cross section, s_{geo}: geometric standard deviation.

Step 2: Finding scale factors from glass beads

Model the theoretical response of the glass bead measurements by assuming a small standard deviation in the size distribution of each bead size (e.g., 10 %). In order to model the σ_F correctly, the refractive indices for all glass beads, as well as the collection angles of the scattering spectrometer, need to be taken into account. Fit a log-normal distribution of the resulting σ_F and find the mode or geometric mean of the distribution (see Fig. A4b).

The scale factor c_F can then be calculated using the relationship $c_F = \sigma_F / I_F$. A scale factor for each calibration size is calculated in this way. For each scale factor, the s_{geo} can be calculated by error-propagating the s_{geo} of the fitted log-normal curves of the measurements, as well as the model (see Fig. A5). Since both distributions, the measurements and the expected

https://doi.org/10.5194/egusphere-2026-3790
Preprint. Discussion started: 6 August 2026

theoretical response, are log-normal, the logarithm of the scale factor c_F is also normally distributed ($\mathcal{N}$) as:

$$\ln c_F \sim \mathcal{N}(\nu_{\mathrm{geo},\sigma_\mathrm{F}} - \nu_{\mathrm{geo},\mathrm{I_F}}, s^2_{\ln \sigma_F} + s^2_{\ln I_F} - 2 s_{\ln \sigma_F} \cdot s_{\ln I_F}) \tag{A4}$$

With ν_{geo} being the geometric mean and s the standard deviation of each distribution in log space. The standard deviation of $\ln c_F$ can be calculated via error propagation:

$$s_{lnc_F} = \sqrt{s^2_{\ln \sigma_F} + s^2_{\ln I_F} - 2 s_{\ln \sigma_F} \cdot s_{\ln I_F}}. \tag{A5}$$

The s_{geo} of the c_F in natural space can then be calculated using:

$$s_{\mathrm{geo},\mathrm{c_F}} = \exp(s_{\ln c_F}). \tag{A6}$$

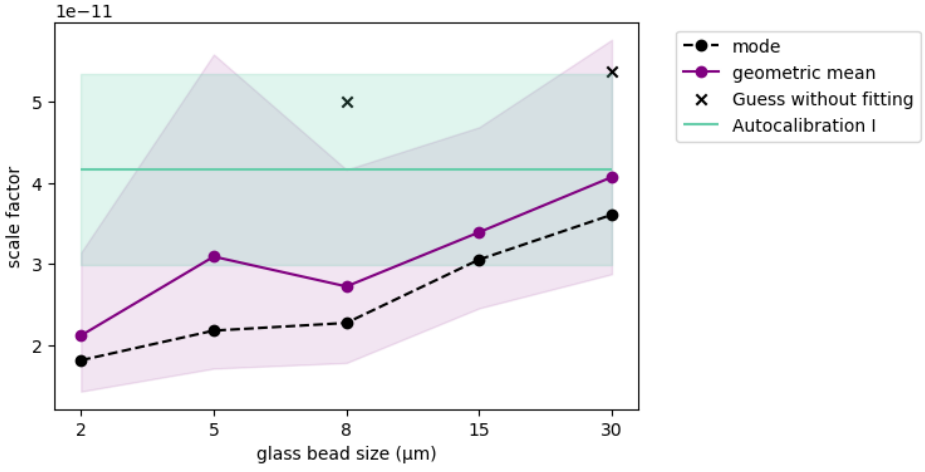

Figure A5. Comparison of scale factors derived from the glass bead calibration. The shaded area corresponds to the geometric standard deviation s_{geo} of the geometric mean (purple line), while retrieved scale factors using the fitted mode is shown as a black dashed line. The result from the autocalibration I (cyan line and shaded standard deviation) is shown for comparison exemplarily over the same size range as the glass beads used here. Black crosses (best guess) indicate how scale factors would look like if the modeled size distribution of the glass beads were not taken into account.

In order to calculate the overall c_F from all calibration beads, a weighted average is performed where $1/s^2_{\mathrm{geo},\mathrm{c_F}}$ is used as a weight. Using the overall c_F, I_F can now be calculated into σ.

Step 3: Mie model

Model the σ of water ($n = 1.33$), for the collection angles of your instrument (here the Ground-based Fog and Aerosol Spectrometer (GFAS), see also Tab. 1) over the expected measurement size range. All Mie-Lorenz calculations (to derive e.g., σ) within this work were performed using the python package PyMieScatt (Sumlin et al., 2018) based on the algorithms of Bohren and Huffman (1998).

https://doi.org/10.5194/egusphere-2026-3790
Preprint. Discussion started: 6 August 2026

Step 4: Regression and diameter assignment

Create a regression between particle size and σ that removes the oscillations in σ, as described in Sect. A2.

Step 5: Final diameter assignment

A diameter can now be calculated. After translating I into σ with step 1 and 2, we can use the relationship established in step 3 and 4 to calculate a diameter to each particle.

https://doi.org/10.5194/egusphere-2026-3790
Preprint. Discussion started: 6 August 2026

Appendix B: Data processing

Within this section, we will describe the individual data processing steps needed to derive reliable observables. This includes the following steps:

1. Attenuation correction*
2. Qualifier-to-sizer ratio filtering*
3. Application of scale factors
4. Assigning particle sizes to individual particles
5. Binning of single-particle data to derive particle size distribution and calculate microphysical parameters
6. Sample loss correction

*only needed for certain GFAS versions built after 2024.

Attenuation correction

A special correction is needed for GFAS versions built after 2024. This version of the GFAS (with one detector gain for each of the four detectors) has a moving baseline in all detectors that is not accounted for when I is passed to the data file. This baseline moves depending on the Full-Width-Half-Maximum (FWHM) of the signal - a function of size and particle velocity (personal comm. ENVEA), leading to a higher baseline with a higher FWHM. The higher baseline results in under-sizing, especially for large particles. To correct for this, ENVEA developed a correction factor CF that must be calculated for each particle in all four detectors:

$$CF = 1 + 0.00404079 \cdot \mathrm{FWHM}^{1.07336} \tag{B1}$$

This empirical correction factor is then multiplied by I in each detector in the PbP data.

Forward scattering qualifier-to-sizer ratio filtering

To ensure that the particle was measured within the DOF of the laser beam, the GFAS automatically excludes particles that do not have a certain ratio between the signal intensities of the qualifier and the sizer (forward) detector. These particles are excluded before the output of the PbP or User files. If the attenuation correction has to be performed, the filtering also has to be applied to particles that now have a ratio falling outside of the expected range. The ratio to accept a particle as measured within the DOF is (Envea, personal communication):

$$\frac{I_\mathrm{Q}}{I_\mathrm{F}} \overset{!}{\geq} 0.6 \tag{B2}$$

with I being the signal intensity for the qualifier (Q) and the forward (F) detector.

https://doi.org/10.5194/egusphere-2026-3790
Preprint. Discussion started: 6 August 2026

Application of scale factors

The scale factors can be calculated via the different calibration methods introduced within this work (Sect. 2.2 and 4.1). The signal intensity I of the individual detectors will then be translated into σ using Eq. (3).

Assigning particle size to individual particles

After translating I into σ for all detectors, the strictly monotonic relationship between particle diameter and σ_F established in Sect. A2 can be used to calculate each particle's d_{opt}.

Binning of single-particle data

As mentioned previously, Mie oscillations lead to the problem that several particle sizes may result in the same measured I. Therefore, the derived particle d_{opt} should be binned in Mie-aware size bins as described in Sect. A2. The bin thresholds (diameter, I, and σ_F) chosen in this work can be found in the SI in Tab. S1.

Sample loss corrections

The particle sampling efficiencies of the GFAS can be divided into three types: (a) aspiration, (b) transmission, and (c) transport (see Spiegel et al., 2012, for more details). In summary, aspiration losses occur when the wind direction and velocity do not align with the orientation of the inlet and its sample flow rate; they describe the ratio between particles entering the inlet and the ambient concentration. This efficiency can only be calculated when the difference between inlet orientation and wind direction is smaller than either 90 or 60 °, depending on the wind speed. Transmission efficiency is the efficiency with which particles make it through the inlet. The transmission efficiency can only be calculated when the difference between inlet orientation and wind direction is smaller than 90 °. Transport losses are gravitational and turbulent losses that occur in the sample tube between the inlet and detector. These losses are independent of wind speed and direction and are only constrained by the turbulence of the airflow. Efficiencies were not taken into account when they were below 0.1, because such a low number would lead to the statistical problem of overestimating something that might not be statistically significant in number. An overview of the availability of the different sampling efficiencies is given in Fig. S5.

https://doi.org/10.5194/egusphere-2026-3790
Preprint. Discussion started: 6 August 2026

Appendix C: Measurement uncertainties and limitations

In the following, GFAS-specific measurement uncertainties will be described, followed by a Root Sum Square (RSS) error estimate for each uncertainty component (Tab. C1). The error estimates were made using an uncertainty propagation analysis through Monte Carlo simulations. For these simulations, a log-normal particle size distribution was used. Random particles were selected from this distribution several million times for each uncertainty condition (listed below). The selected particle is represented by its scattering cross section converted to signal intensity (I) and then classified into an equivalent optical diameter (d_{opt}). This derived d_{opt} is compared with the physical geometric diameter to calculate the sizing errors over the size range of the GFAS.

Collection Angle

The collection angles are determined by the optical geometry and location of the particle in the beam. The uncertainty in collection angles propagates into the derivation of size from Mie-Lorenz theory, which requires the collection angle as an input. The sources of systematic errors are the uncertainties in the dimensions of the right-angle mirror $(\pm 0.2mm)$, objective lens ($\pm$ 0.5 mm), and the location of the center of focus ($\pm$ 1 mm). The random error originates from uncertainties in where particles pass through the beam relative to the center of focus ($\pm$ 1 mm). The random errors depend on particle diameter.

Beam intensity non-uniformity

The laser beam used in the GFAS has a Gaussian intensity distribution. There is no systematic error, but there is a random error, given that the location where the particles pass through the beam depends on their spatial separations in the sampled air. The qualifier's optical mask constrains the detection region so that more than 95% of qualified particles pass through the laser beam where the intensity is $> 85\%$ of the maximum. This is also somewhat dependent on the particle's size.

Mie-Lorenz theory

The uncertainties due to the non-monotonic nature of Mie-Lorenz scattering are dependent on the size range, refractive index and wavelength of the incident light. The errors are considered neither systematic or random here because the theory is quite clear with respect to scattering intensity versus size, the error is how this is interpreted if an inversion to the data is not done, i.e., if more than one particle size has the same scattering intensity, the software does not *a priori* know to which size the scattering intensity should be assigned to. Since it doesn't matter which type of error this is in the final calculation of RSS, it will be considered random here.

Refractive index

The uncertainties related to the particle refractive index fall into two categories: 1) natural and 2) calibration. The uncertainties related to the first category refer to how we interpret the data, i.e., the uncertainty due to how we derive a particle size from the scattering signal. This error can be quite large, depending on the difference between the assumed and actual refractive index.

https://doi.org/10.5194/egusphere-2026-3790
Preprint. Discussion started: 6 August 2026

These uncertainties are intrinsically embedded in the analysis of error through Mie-Lorenz theory, which was calculated over a range of refractive indices with real parts from 1.33 to 1.80 and imaginary components from $0.0i$ to $0.01i$.

The second type of refractive index uncertainty is a result of variations in the refractive index of reference particles used to calibrate the GFAS. The manufacturers of these particles list the refractive index at a specific wavelength that is close to, but not the same as, the GFAS. In addition, an investigation into the refractive index of crown glass beads, for example, showed published values between 1.51 and 1.54 at a wavelength of 658 nm. The Monte Carlo simulation of this uncertainty, introduced to the calibration process, leads to the uncertainties shown in (Tab. C1)

Electronic noise

The term noise refers to any random background electrical or light signals that contribute to the voltage signals from the detectors. These random pulses are removed by the algorithm that calculates a running average of the signal baseline, which is then subtracted from the peak before assigning a size. In the GFAS, this baseline generally varies between 1000 and 5000 Analog to Digital Counts out of a maximum possible count of 131000.

Coincidence

There is a finite probability, even at small concentrations, that the spacing between particles arriving in the laser beam is smaller than the width of the laser beam. In these cases, the light scattered is some combination of scattering from the two (or more) particles in the beam. This will lead to an overestimate in size, but one that is difficult to quantify. However, the probability that coincidence occurs (P_c) increases with particle number concentration N and can be quantified via (Baumgardner et al., 1985):

$$P_\mathrm{c} = 1 - \exp\left(-\frac{d_\mathrm{beam}}{N^{-1/3}}\right), \tag{C1}$$

with the cross section of the laser beam d_beam. For P_c to be below, e.g., 20 %, N has to be below 1000 cm^{-3} (Fig. C1).

https://doi.org/10.5194/egusphere-2026-3790
Preprint. Discussion started: 6 August 2026

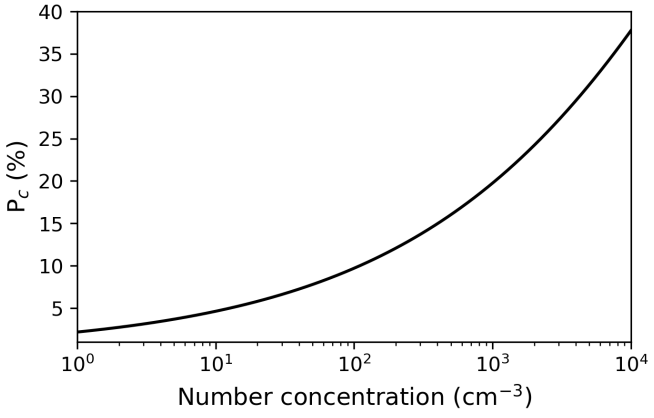

Figure C1. Probability of particle coincidence P_c calculated for the GFAS. Coincidence here means that the distance between two particles crossing the laser beam is smaller than the laser cross section.

Table C1. Equivalent Optical Diameter Root Sum Square (RSS) Error Analysis (Taylor and Kuyatt, 1994) for the different measurement uncertainties within the GFAS.

Source	**Size range**	**Systematic error (%)**	**Random error (%)**
Collection Angle	$\leq 12\ \mu$m	$\pm$(2–5)	$\pm$(2–5)
	$> 12\ \mu$m	< 8	< 5
Beam intensity non-uniformity	-	-	± 15
Mie-Lorenz theory	$< 10\ \mu$m	-	$\pm$(5–60)
	$> 10\ \mu$m	-	± 3
Refractive index	$< 10\ \mu$m	-	± 15
Electronic noise	-	-	$\pm$0.5–4
Coincidence	-	-	< 5
Overall uncertainty (RSS)	$\leq 12\ \mu$m		$\pm$(16–102)
	$> 12\ \mu$m		± 18

Code availability. The code behind the analysis and needed for the GFAS calibration can be found on our department's GitHub page https://github.com/SU-air/instrumentation-GFAS.

Data availability. The data will be available on the Bolin Center Data Base (bolin.su.se/data) and uploaded during the review process.

https://doi.org/10.5194/egusphere-2026-3790
Preprint. Discussion started: 6 August 2026

Author contributions. Conceptualization: DB and PZ; Data curation: LH, DB, CZ and CM; Formal analysis: LH and DB; Funding acquisition: IR; Investigation: LH, DB, CZ, CM and PZ; Methodology: LH, DB, DH, AN and PZ; Project administration: CZ, ZK, CM and PZ; Resources: ZK, CM, IR, RK and PZ; Software: LH, JL, DB and DH; Supervision: IR, RK and PZ; Validation: LH, JL and DB; Visualization: LH; Writing - Original Draft: LH, DB and PZ; Writing - Review & Editing: LH, DB, DH, JL, AN, CZ, ZK, CM, IR, RK and PZ;

Competing interests. One author is member of the editorial board of AMT. DB is a co-founder of DMT, which developed and commercially markets the instruments used in this study. DH is employed by DMT (now Envea). The remaining authors declare no competing interests.

Acknowledgements. This work was supported by the European Research Council (Consolidator Grant INTEGRATE 865799) and the Knut and Alice Wallenberg Foundation (Grant 2021.0169 and 2021.0298). The observations at SBO were part of a Transnational access project that is supported by the European Commission under the Horizon 2020 – Research and Innovation Framework Programme, H2020-INFRAIA-2020-1, ATMO-ACCESS Grant Agreement number: 101008004.

AI has been used to assist and help in coding and for minor language (grammar) adjustments. No generative text from AI was used.

https://doi.org/10.5194/egusphere-2026-3790
Preprint. Discussion started: 6 August 2026

References

Baumgardner, D.: An analysis and comparison of five water droplet measuring instruments, Journal of Climate and Applied Meteorology, pp. 891–910, 1983.

Baumgardner, D., Strapp, W., and Dye, J. E.: Evaluation of the Forward Scattering Spectrometer Probe. Part II: Corrections for Coincidence and Dead-Time Losses, Journal of Atmospheric and Oceanic Technology, 2, 626–632, https://doi.org/10.1175/1520-0426(1985)002<0626:EOTFSS>2.0.CO;2, 1985.

Baumgardner, D., Dye, J. E., Gandrud, B., Barr, K., Kelly, K., and Chan, K. R.: Refractive indices of aerosols in the upper troposphere and lower stratosphere, Geophysical Research Letters, 23, 749–752, https://doi.org/10.1029/96GL00707, 1996.

Baumgardner, D., Brenguier, J., Bucholtz, A., Coe, H., DeMott, P., Garrett, T., Gayet, J., Hermann, M., Heymsfield, A., Korolev, A., Krämer, M., Petzold, A., Strapp, W., Pilewskie, P., Taylor, J., Twohy, C., Wendisch, M., Bachalo, W., and Chuang, P.: Airborne instruments to measure atmospheric aerosol particles, clouds and radiation: A cook's tour of mature and emerging technology, Atmospheric Research, 102, 10–29, https://doi.org/10.1016/j.atmosres.2011.06.021, 2011.

Bohren, C. F. and Huffman, D. R.: Absorption and scattering of light by small particles, John Wiley & Sons, 1998.

Burnet, F. and Brenguier, J.: Validation of droplet spectra and liquid water content measurements, Physics and Chemistry of the Earth, Part B: Hydrology, Oceans and Atmosphere, 24, 249–254, https://doi.org/10.1016/S1464-1909(98)00046-X, 1999.

Collaud Coen, M., Weingartner, E., Schaub, D., Hueglin, C., Corrigan, C., Henning, S., Schwikowski, M., and Baltensperger, U.: Saharan dust events at the Jungfraujoch: detection by wavelength dependence of the single scattering albedo and first climatology analysis, Atmospheric Chemistry and Physics, 4, 2465–2480, https://doi.org/10.5194/acp-4-2465-2004, 2004.

Cotterell, M. I., Willoughby, R. E., Bzdek, B. R., Orr-Ewing, A. J., and Reid, J. P.: A complete parameterisation of the relative humidity and wavelength dependence of the refractive index of hygroscopic inorganic aerosol particles, Atmospheric Chemistry and Physics, 17, 9837–9851, https://doi.org/10.5194/acp-17-9837-2017, 2017.

Cotton, R., Osborne, S., Ulanowski, Z., Hirst, E., Kaye, P. H., and Greenaway, R. S.: The Ability of the Small Ice Detector (SID-2) to Characterize Cloud Particle and Aerosol Morphologies Obtained during Flights of the FAAM BAe-146 Research Aircraft, Journal of Atmospheric and Oceanic Technology, 27, 290–303, https://doi.org/10.1175/2009JTECHA1282.1, 2010.

Doulgeris, K.-M., Komppula, M., Romakkaniemi, S., Hyvärinen, A.-P., Kerminen, V.-M., and Brus, D.: In situ cloud ground-based measurements in the Finnish sub-Arctic: intercomparison of three cloud spectrometer setups, Atmospheric Measurement Techniques, 13, 5129–5147, https://doi.org/10.5194/amt-13-5129-2020, 2020.

Farias, G., Vasconcelos, E., Cesar, S., and Maradudin, A.: Mie scattering by a perfectly conducting sphere with a rough surface, Physica A: Statistical Mechanics and its Applications, 207, 315–322, https://doi.org/10.1016/0378-4371(94)90389-1, 1994.

Fugal, J. P., Shaw, R. A., Saw, E. W., and Sergeyev, A. V.: Airborne digital holographic system for cloud particle measurements, Applied Optics, 43, 5987, https://doi.org/10.1364/AO.43.005987, 2004.

Gayet, J. F., Crepel, O., Fournol, J. F., and Oshchepkov, S.: A new airborne polar Nephelometer for the measurements of optical and microphysical cloud properties. Part I: Theoretical design, Annual Geophysicae, 1996.

Gerber, H.: Direct measurement of suspended particulate volume concentration and far-infrared extinction coefficient with a laser-diffraction instrument, Applied Optics, 30, 4824, https://doi.org/10.1364/AO.30.004824, 1991.

https://doi.org/10.5194/egusphere-2026-3790
Preprint. Discussion started: 6 August 2026

Glen, A. and Brooks, S. D.: A new method for measuring optical scattering properties of atmospherically relevant dusts using the Cloud and Aerosol Spectrometer with Polarization (CASPOL), Atmospheric Chemistry and Physics, 13, 1345–1356, https://doi.org/10.5194/acp-13-1345-2013, 2013.

Glen, A. and Brooks, S. D.: Single Particle Measurements of the Optical Properties of Small Ice Crystals and Heterogeneous Ice Nuclei, Aerosol Science and Technology, 48, 1123–1132, https://doi.org/10.1080/02786826.2014.963023, 2014.

Gultepe, I., Isaac, G. A., Joe, P., Kucera, P. A., Theriault, J. M., and Fisico, T.: Roundhouse (RND) Mountain Top Research Site: Measurements and Uncertainties for Winter Alpine Weather Conditions, Pure and Applied Geophysics, 171, 59–85, https://doi.org/10.1007/s00024-012-0582-5, 2014.

Knollenberg, R. G.: Three new instruments for cloud physics measurements: The 2-D spectrometer, the Forward Scattering Spectrometer Probe, and the active scattering aerosol spectrometer., American Meteorological Society, Preprints, Int. Conf. on Cloud Physics, 554–561, 1976.

Korolev, A., McFarquhar, G., Field, P. R., Franklin, C., Lawson, P., Wang, Z., Williams, E., Abel, S. J., Axisa, D., Borrmann, S., Crosier, J., Fugal, J., Krämer, M., Lohmann, U., Schlenczek, O., Schnaiter, M., and Wendisch, M.: Mixed-Phase Clouds: Progress and Challenges, Meteorological Monographs, 58, 5.1–5.50, https://doi.org/10.1175/AMSMONOGRAPHS-D-17-0001.1, 2017.

Liou, K.-N.: An introduction to atmospheric radiation, no. v. 84 in International geophysics series, Academic Press, Amsterdam ; Boston, 2nd ed edn., 2002.

Lorenz, L. V.: Lysbevægelsen i og uden for en af plane Lysbølger belyst Kugle, The Royal Danish Academy of Sciences and Letters, 1890.

Mahrt, F., Wieder, J., Dietlicher, R., Smith, H. R., Stopford, C., and Kanji, Z. A.: A high-speed particle phase discriminator (PPD-HS) for the classification of airborne particles, as tested in a continuous flow diffusion chamber, Atmospheric Measurement Techniques, 12, 3183–3208, https://doi.org/10.5194/amt-12-3183-2019, 2019.

McFarquhar, G. M., Um, J., Freer, M., Baumgardner, D., Kok, G. L., and Mace, G.: Importance of small ice crystals to cirrus properties: Observations from the Tropical Warm Pool International Cloud Experiment (TWP-ICE): SMALL ICE CRYSTALS IN TROPICAL CIRRUS, Geophysical Research Letters, 34, n/a–n/a, https://doi.org/10.1029/2007GL029865, 2007.

Mie, G.: Beiträge zur Optik trüber Medien, speziell kolloidaler Metallösungen, Annalen der Physik, 330, 377–445, https://doi.org/10.1002/andp.19083300302, 1908.

Miles, N. L., Verlinde, J., and Clothiaux, E. E.: Cloud Droplet Size Distributions in Low-Level Stratiform Clouds, Journal of the Atmospheric Sciences, 57, 295–311, https://doi.org/10.1175/1520-0469(2000)057<0295:CDSDIL>2.0.CO;2, 2000.

Nichman, L., Fuchs, C., Järvinen, E., Ignatius, K., Höppel, N. F., Dias, A., Heinritzi, M., Simon, M., Tröstl, J., Wagner, A. C., Wagner, R., Williamson, C., Yan, C., Connolly, P. J., Dorsey, J. R., Duplissy, J., Ehrhart, S., Frege, C., Gordon, H., Hoyle, C. R., Kristensen, T. B., Steiner, G., McPherson Donahue, N., Flagan, R., Gallagher, M. W., Kirkby, J., Möhler, O., Saathoff, H., Schnaiter, M., Stratmann, F., and Tomé, A.: Phase transition observations and discrimination of small cloud particles by light polarization in expansion chamber experiments, Atmospheric Chemistry and Physics, 16, 3651–3664, https://doi.org/10.5194/acp-16-3651-2016, 2016.

Pinnick, R. and Auvermann, H.: Response characteristics of knollenberg light-scattering aerosol counters, Journal of Aerosol Science, 10, 55–74, https://doi.org/10.1016/0021-8502(79)90136-8, 1979.

Renard, J.-B., Dulac, F., Berthet, G., Lurton, T., Vignelles, D., Jégou, F., Tonnelier, T., Jeannot, M., Couté, B., Akiki, R., Verdier, N., Mallet, M., Gensdarmes, F., Charpentier, P., Mesmin, S., Duverger, V., Dupont, J.-C., Elias, T., Crenn, V., Sciare, J., Zieger, P., Salter, M., Roberts, T., Giacomoni, J., Gobbi, M., Hamonou, E., Olafsson, H., Dagsson-Waldhauserova, P., Camy-Peyret, C., Mazel, C., Décamps, T., Piringer, M., Surcin, J., and Daugeron, D.: LOAC: a small aerosol optical counter/sizer for ground-based and balloon measurements of the size

https://doi.org/10.5194/egusphere-2026-3790
Preprint. Discussion started: 6 August 2026

distribution and nature of atmospheric particles – Part 1: Principle of measurements and instrument evaluation, Atmospheric Measurement Techniques, 9, 1721–1742, https://doi.org/10.5194/amt-9-1721-2016, 2016.

Rosenberg, P. D., Dean, A. R., Williams, P. I., Dorsey, J. R., Minikin, A., Pickering, M. A., and Petzold, A.: Particle sizing calibration with refractive index correction for light scattering optical particle counters and impacts upon PCASP and CDP data collected during the Fennec campaign, Atmospheric Measurement Techniques, 5, 1147–1163, https://doi.org/10.5194/amt-5-1147-2012, 2012.

Schauer, G. and Maier, C.: SBO 1230 Aerosol SCT coefficients Version 1, https://data.sonnblick.net/dataset/d6870b43, 2020.

Schotland, R. M., Sassen, K., and Stone, R.: Observations by Lidar of Linear Depolarization Ratios for Hydrometeors, Journal of Applied Meteorology, 10, 1011–1017, https://doi.org/10.1175/1520-0450(1971)010<1011:OBLOLD>2.0.CO;2, 1971.

Shepherd, R. H., King, M. D., Marks, A. A., Brough, N., and Ward, A. D.: Determination of the refractive index of insoluble organic extracts from atmospheric aerosol over the visible wavelength range using optical tweezers, Atmospheric Chemistry and Physics, 18, 5235–5252, https://doi.org/10.5194/acp-18-5235-2018, 2018.

Shupe, M. D., Daniel, J. S., De Boer, G., Eloranta, E. W., Kollias, P., Long, C. N., Luke, E. P., Turner, D. D., and Verlinde, J.: A Focus On Mixed-Phase Clouds: The Status of Ground-Based Observational Methods, Bulletin of the American Meteorological Society, 89, 1549–1562, https://doi.org/10.1175/2008BAMS2378.1, 2008.

Spiegel, J. K., Zieger, P., Bukowiecki, N., Hammer, E., Weingartner, E., and Eugster, W.: Evaluating the capabilities and uncertainties of droplet measurements for the fog droplet spectrometer (FM-100), Atmospheric Measurement Techniques, 5, 2237–2260, https://doi.org/10.5194/amt-5-2237-2012, 2012.

Sumlin, B. J., Heinson, W. R., and Chakrabarty, R. K.: Retrieving the aerosol complex refractive index using PyMieScatt: A Mie computational package with visualization capabilities, Journal of Quantitative Spectroscopy and Radiative Transfer, 205, 127–134, https://doi.org/10.1016/j.jqsrt.2017.10.012, 2018.

Taylor, B. N. and Kuyatt, C. E.: Guidelines for evaluating and expressing the uncertainty of NIST measurement results, vol. 1297, US Department of Commerce, Technology Administration, National Institute of . . . , 1994.

Tiitta, P., Leskinen, A., Kaikkonen, V. A., Molkoselkä, E. O., Mäkynen, A. J., Joutsensaari, J., Calderon, S., Romakkaniemi, S., and Komppula, M.: Intercomparison of holographic imaging and single-particle forward light scattering in situ measurements of liquid clouds in changing atmospheric conditions, Atmospheric Measurement Techniques, 15, 2993–3009, https://doi.org/10.5194/amt-15-2993-2022, 2022.

Um, J. and McFarquhar, G. M.: Dependence of the single-scattering properties of small ice crystals on idealized shape models, Atmospheric Chemistry and Physics, 11, 3159–3171, https://doi.org/10.5194/acp-11-3159-2011, 2011.

Zenker, J., Collier, K. N., Xu, G., Yang, P., Levin, E. J. T., Suski, K. J., DeMott, P. J., and Brooks, S. D.: Using depolarization to quantify ice nucleating particle concentrations: a new method, Atmospheric Measurement Techniques, 10, 4639–4657, https://doi.org/10.5194/amt-10-4639-2017, 2017.

Zhao, G., Li, F., and Zhao, C.: Determination of the refractive index of ambient aerosols, Atmospheric Environment, 240, 117 800, https://doi.org/10.1016/j.atmosenv.2020.117800, 2020.